Observation-Constrained Climate Change in China over 1850–2014 by Aerosols in CMIP6 Models

ZHUOFAN QIN[a] AND HONG LIAO[a]

[a] *Jiangsu Key Laboratory of Atmospheric Environment Monitoring and Pollution Control, Jiangsu Collaborative Innovation Center of Atmospheric Environment and Equipment Technology, School of Environmental Science and Engineering, Nanjing University of Information Science and Technology, Nanjing, Jiangsu, China*

(Manuscript received 10 April 2024, in final form 12 August 2024, accepted 27 September 2024)

ABSTRACT: Aerosols play a very important role in climate change with large uncertainties. Using the multimodel results from CMIP6, we analyzed the aerosol effective radiative forcing (ERF) and aerosol-induced surface air temperature (SAT) change in China in the present day (PD; 11-yr mean of 2004–14) relative to the preindustrial (PI) time (11-yr mean of 1850–60). With the increase in the anthropogenic emissions, the simulated surface $PM_{2.5}$ concentration and aerosol optical depth (AOD) averaged over eastern China (EC; 18°–44°N, 103°–122°E) increased by 21.43 ± 7.58 $\mu g\ m^{-3}$ and 0.47 ± 0.33, respectively, from PI to PD. The simulated aerosol ERFs in EC were −4.91 ± 2.56 and −5.35 ± 2.40 W m^{-2} from equilibrium and transient simulations, respectively. The simulated change in SAT caused by the increases in aerosols was −1.37° ± 0.38°C in EC from PI to PD. The simulated values of equilibrium and transient climate sensitivity to aerosols (CSA; aerosol-induced SAT change per unit aerosol ERF) in EC were 0.236° and 0.222°C (W $m^{-2})^{-1}$, respectively. By using the observed AOD from MODIS to constrain aerosol ERF, the constrained aerosol equilibrium and transient ERFs over EC were −4.66 and −4.93 W m^{-2}, respectively, which were smaller in magnitude than the simulated values directly from the models. By using the observed SAT from the Climatic Research Unit temperature version 5 to constrain aerosol-induced cooling, the surface cooling caused by aerosols was magnified to −1.47°C. The adjusted CSA after the constraint was calculated by dividing adjusted aerosol-induced SAT change by adjusted aerosol ERF. Adjusted equilibrium and transient CSA values in EC were 0.32° and 0.34°C (W $m^{-2})^{-1}$, respectively.

KEYWORDS: Aerosols; Climate sensitivity; Radiative forcing; Climate models

1. Introduction

Atmospheric aerosols exert significant influences on atmospheric visibility, human health, ecosystems, and climate change. Aerosols affect Earth's radiative balance directly by scattering and absorbing solar radiation and indirectly by modifying cloud properties, resulting in an overall negative radiative forcing (Boucher et al. 2013). During the period from 1750 to 2019, the cooling effect attributed to the increases in aerosol concentrations offset approximately 31.6% of the positive radiative forcing induced by the increases in well-mixed greenhouse gases (GHGs) (Myhre et al. 2013a).

Radiative forcing serves as a valuable metric for assessing the contribution of specific atmospheric components to climate change. Previous studies (Chang and Liao 2009; Chang et al. 2009, 2015; Dang and Liao 2019; Li et al. 2013, 2014; Li et al. 2016; Qian et al. 2003) examined the direct radiative forcing (DRF; the scattering and absorption of radiation) by aerosols in China and reported that DRF values at the top of the atmosphere (TOA) or the tropopause over China largely exceeded the global mean. Since the Fifth Assessment Report of the Intergovernmental Panel on Climate Change, effective radiative forcing (ERF) has gained prominence for quantifying climate drivers, encompassing DRF, semidirect climate effect, and indirect climate effect of aerosols. ERF is defined as the change in net downward radiative flux at the TOA, accounting for adjustments in atmospheric temperature, water vapor, cloud, and land albedo while keeping the ocean/sea ice conditions constant (Myhre et al. 2013a). Several studies reported that the global mean anthropogenic aerosol ERF (AERF) values were in the range of −2.49 to −1.09 W m^{-2} by using a single model (Grandey et al. 2018; Michou et al. 2020; O'Connor et al. 2021; Oshima et al. 2020; Wang et al. 2020; Zhang et al. 2016. See details in Table S1 in the online supplemental material).

Estimates of ERF have large uncertainties depending on models' representation of aerosols and their radiative properties. To reduce the uncertainties associated with a single model, the multimodel results were provided by phase 6 of the Coupled Model Intercomparison Project (CMIP6) (Eyring et al. 2016). One of the CMIP6-Endorsed Model Intercomparison Projects, the Radiative Forcing Model Intercomparison Project (RFMIP) (Pincus et al. 2016), diagnosed model ERF by specifying sea surface temperatures and sea ice conditions. Zanis et al. (2020) used RFMIP time-slice simulations from 10 Earth system models or general circulation models and obtained a global annual mean aerosol ERF of −1.00 W m^{-2} in the present day (2014) relative to the preindustrial period (1850), with the largest negative ERF value over East Asia (about −5 W m^{-2}). Smith et al. (2021) presented ERF obtained from transient simulations of 11 CMIP6 models and

Supplemental information related to this paper is available at the Journals Online website: https://doi.org/10.1175/JCLI-D-24-0204.s1.

Corresponding author: Hong Liao, hongliao@nuist.edu.cn

DOI: 10.1175/JCLI-D-24-0204.1

showed that the negative global mean aerosol ERF reached a peak of −1.50 W m^{-2} around 1980.

Climate models exhibit uncertainties in simulating climate change. The uncertainty of unobservable climate variables can be constrained by the contemporary measurements of the observable parameters using the statistical relationship between them (Cherian et al. 2014; Klein and Hall 2015; Watson-Parris et al. 2020). Based on the relationship between the present-day total aerosol optical depth (AOD) and the historical change in anthropogenic AOD across three different model ensembles, Watson-Parris et al. (2020) used satellite-based observations of present-day total AOD to constrain the historical changes in anthropogenic AOD and further reported a constrained global clear-sky DRF of −0.69 W m^{-2}. Smith et al. (2021) constrained the global historical aerosol ERF by assigning weights to a vast array of model ensemble members based on their ability to reproduce observed near-surface warming and ocean heat uptake and found that the best estimation of aerosol ERF was −1.1 W m^{-2} for 2005–14 relative to 1750.

Previous studies have estimated the contributions of human activities to historical climate change by conducting single-factor forcing simulations within the Detection and Attribution Model Intercomparison Project (DAMIP) (Gillett et al. 2016) in CMIP6 (Nie et al. 2019; Samset 2022; Smith and Forster 2021). On this basis, combined with the regression-based optimal fingerprinting approach, detection and attribution (D&A) analysis has been used to quantify the contributions of individual forcings to the observed climate change (Allen and Tett 1999; Barnett et al. 2005; Li et al. 2021; Seong et al. 2021; Xu et al. 2015; Yu et al. 2022; Zhang et al. 2013). For example, Li et al. (2021), by using the D&A analysis, estimated that anthropogenic GHGs and aerosols contributed 1.8° and −0.7°C, respectively, to the observed terrestrial warming of about 1.5°C between 1850–1900 and 2011–20. Seong et al. (2021) reported an observed increase in global and annual mean maximum daily temperature of 0.96 K during 1951–2015, in which 1.76 K was attributed to the increases in GHGs and −0.88 K was attributed to the increases in aerosols.

Existing studies on aerosol ERF and its climate effect in China primarily relied on single models or single chemical components (Archer-Nicholls et al. 2019; Chen et al. 2020; Gao et al. 2022; Hu and Sun 2022; Liu et al. 2023; Liu et al. 2022; Seo et al. 2020; Tang et al. 2020; Wang et al. 2022). By using the WRF-Chem model, Archer-Nicholls et al. (2019) estimated a TOA ERF of 1.22 W m^{-2} from residential sector aerosols (mainly black carbon) over eastern China in January 2014. By using the atmosphere model of the Community Earth System Model, version 2 (CESM2), Liu et al. (2023) reported that the Air Pollution Prevention and Control Action Plan in China over 2013–17 led to a positive aerosol ERF of 1.59 W m^{-2} and consequently a 0.09°C warming in summer over central-eastern China (25°–40°N, 105°–122.5°E). By carrying out simulations using the U.K.'s Earth System Model, version 1 (UKESM1), Seo et al. (2020) showed aerosol ERF of −3.87 W m^{-2} over eastern–central China (19°–41°N, 101°–130°E) in 1980–2010 relative to 1850. Combining observed shortwave absorption and model simulation, Liu et al. (2022) identified an emergent constraint on aerosol absorption optical depth of anthropogenic black carbon and provided an observationally constrained TOA black carbon ERF of 2.4–3.0 W m^{-2} from aerosol–radiation interaction over China in 2014 relative to 1850.

As reviewed above, the climate effect of aerosols is of utmost importance in the context of climate change, but the relevant multimodel results were mostly global studies without details for China, and the research for the China domain was limited to a single model or a single chemical component. There has been a lack of studies on long-term historical aerosol changes, ERF, and associated temperature responses and climate sensitivity in China based on CMIP6. Most importantly, few studies constrained model-simulated results using observations. In this work, we use results from experiments conducted as part of CMIP6 to make an assessment of historical climate change by aerosols in China from 1850 to 2014. As illustrated in Fig. 1, we initially present the historical change in aerosol concentrations and AOD (section 3a). Subsequently, we analyze aerosol ERF (from both equilibrium and transient simulations; section 3b), followed by the aerosol-induced change in surface air temperature (SAT; section 3c) and the climate sensitivity to aerosols (CSA; section 3d). Additionally, we employ observational data to constrain the outcomes of the model simulations and get the adjusted aerosol ERF, aerosol-induced SAT change, and CSA by using the observed AOD and SAT (section 3e).

2. Data and methods

a. CMIP6 simulations

In this work, we use results of CMIP6 simulations from 10 models, namely, ACCESS-CM2, ACCESS-ESM1-5, CanESM5, CESM2, GFDL-ESM4, GISS-E2-1-G, HadGEM3-GC3.1-LL, IPSL-CM6A-LR, MIROC6, and NorESM2-LM (Table 1) that participated in both RFMIP and DAMIP. RFMIP can provide the estimates of aerosol historical ERF, and DAMIP can provide the historical change in surface temperature induced by aerosol ERF. Model outputs are available on the Earth System Grid Federation (ESGF; https://esgf-node.llnl.gov/search/cmip6/).

The simulated historical monthly data such as aerosol concentrations, AOD at 550 nm, and near-surface (usually 2 m) air temperature (SAT) for 1850–2014 were obtained from the historical simulations (all-forcing simulations of the recent past; experiment id: historical) in CMIP6 (see Table S2 for a detailed list of variables). However, not all the models in CMIP6 had direct outputs of $PM_{2.5}$. To ensure consistency across models, concentrations of $PM_{2.5}$ were calculated as the sum of the dry aerosol mass of sulfate (SO_4^{2-}), nitrate (NO_3^-), ammonium (NH_4^+), organic aerosol (OA), black carbon (BC), sea salt (SS; with a factor of 0.25), and dust (DU; with a factor of 0.1), following the equation $PM_{2.5} = SO_4^{2-} + NO_3^- + NH_4^+ + OA + BC + 0.1 \times DU + 0.25 \times SS$ as in previous studies (Allen et al. 2020; Turnock et al. 2020; Xu et al. 2022). This equation assumes that 100% of SO_4^{2-}, NO_3^-, NH_4^+, OA, and BC are fine mode, whereas 25% of the sea salt and 10% of the dust are fine mode. The historical change in each variable mentioned in this study refers to the difference (denoted

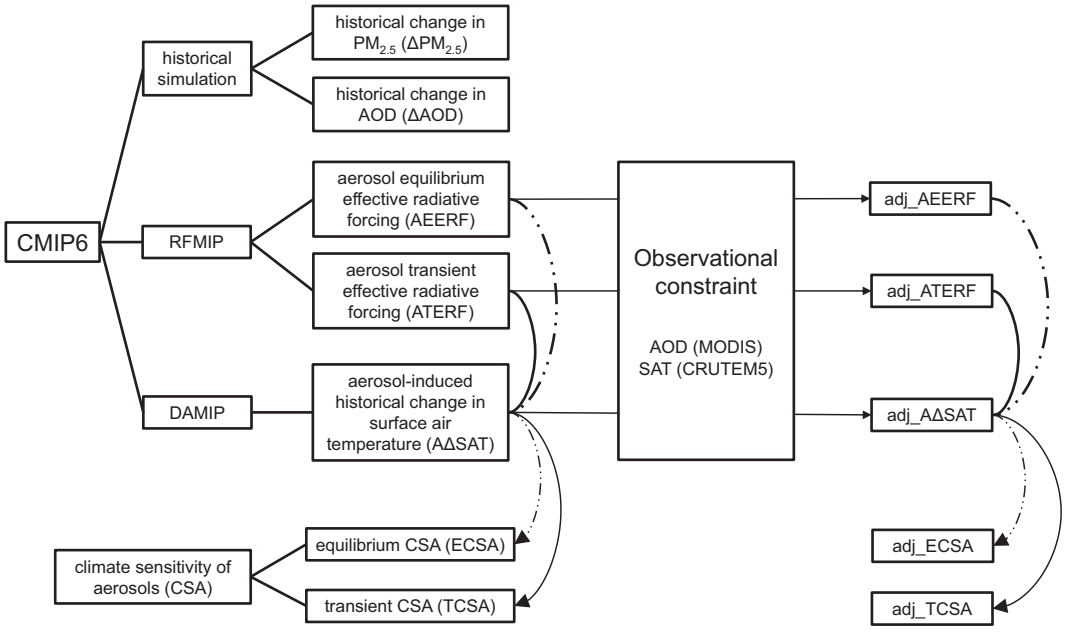

FIG. 1. Framework and main contents in this study. Details of model simulations are shown in section 2a, and approaches of constrain by using observations are described in section 2e.

by symbol Δ) between the present day (PD; 11-yr mean of 2004–14) and the preindustrial (PI) time (11-yr mean of 1850–60) unless otherwise stated.

The estimates of ERF were provided by RFMIP (Pincus et al. 2016) through two types of simulations (time-slice simulations and transient simulations). In time-slice simulations (experiment id: piClim-* in Table 2), forcing agents were held constant at the present-day (year 2014) values for at least 30 years, and the present-day ERF was calculated as the difference in net downward radiative flux at the TOA between the perturbed and control runs (30-yr running means). For simulations with a duration longer than 30 years, the latest 30 years were selected. Such ERF is called equilibrium ERF (EERF). Transient simulations (experiment id: piClim-hist* in Table 2) were designed to capture the historical transient ERF in CMIP6, where the forcing agent concentrations evolved over time. The present-day ERF in transient simulations was calculated as the change in net downward radiative

TABLE 1. Information of 10 CMIP6 models and main available data used in this study. The symbol Δ denotes historical change in PD (11-yr mean of 2004–14) relative to the PI period (11-yr mean of 1850–60). AΔSAT is aerosol-induced historical change in surface air temperature. The symbol √ denotes that the corresponding variable results are available from the model. Concentrations of $PM_{2.5}$ are calculated as $PM_{2.5} = SO_4^{2-} + NO_3^- + NH_4^+ + OA + BC + 0.1 \times DU + 0.25 \times SS$. The term "opd" denotes the direct output of $PM_{2.5}$ from the models.

Model	Horizontal resolution (latitude × longitude)	$\Delta PM_{2.5}$ (opd)	ΔAOD	AEERF	ATERF	AΔSAT
ACCESS-CM2 (Bi et al. 2020)	1.25° × 1.875°		√	√		√
ACCESS-ESM1-5 (Bi et al. 2013; Law et al. 2017; Ziehn et al. 2020)	1.25° × 1.875°		√	√		√
CanESM5 (Swart et al. 2019)	2.8° × 2.8°		√	√	√	√
CESM2 (Danabasoglu et al. 2020; Emmons et al. 2020)	0.94° × 1.25°	√	√	√		√
GFDL-ESM4 (Dunne et al. 2020; Horowitz et al. 2020)	1° × 1.25°	√(√)	√	√		√
GISS-E2-1-G (Kelley et al. 2020)	2° × 2.5°	√(√)	√	√	√	√
HadGEM3-GC3.1-LL (Kuhlbrodt et al. 2018)	1.25° × 1.875°	√	√	√	√	√
IPSL-CM6A-LR (Lurton et al. 2020)	1.26° × 2.5°		√	√	√	√
MIROC6 (Tatebe et al. 2019)	1.4° × 1.4°	√(√)	√	√	√	√
NorESM2-LM (Seland et al. 2020)	1.875° × 2.5°	√(√)	√	√	√	√
Sum	10	6(4)	10	10	6	10

TABLE 2. The experimental design of RFMIP (Pincus et al. 2016) and DAMIP (Gillett et al. 2016) considered in this study.

MIP	Experiment ID	Experiment description	Major purposes for this study
RFMIP	piClim-control	Preindustrial climatology control simulations for at least 30 years	Baseline for model-specific ERF calculations
	piClim-anthro	The same as piClim-control, but with present-day (2014) anthropogenic forcings (GHGs, aerosols, and land use)	Quantify present-day (2014) total anthropogenic ERF
	piClim-aer	The same as piClim-control, but with present-day (2014) aerosols	Quantify present-day (2014) ERF by aerosols
	piClim-ghg	The same as piClim-control, but with present-day (2014) GHGes	Quantify present-day (2014) ERF by GHGes
	piClim-histall	Preindustrial climatology simulations with time-varying forcing by all agents from 1850 to 2014	Diagnose transient ERF from all agents
	piClim-histaer	The same as piClim-histall, but with time-varying anthropogenic aerosols only	Diagnose transient ERF by aerosols
	piClim-histghg	The same as piClim-histall, but with time-varying GHGes only	Diagnose transient ERF by GHGes
	piClim-histnat	The same as piClim-histall, but with time-varying natural forcings (volcanoes and solar variability) only	Diagnose transient ERF by natural forcings
DAMIP	hist-aer	Anthropogenic-aerosol-only historical simulations from 1850 to 2014	Estimate the historical change in air temperature caused by aerosols
	hist-GHG	Greenhouse gas–only historical simulations from 1850 to 2014	Estimate the historical change in air temperature caused by GHGes
	hist-nat	Natural-only historical simulations from 1850 to 2014	Estimate the historical change in air temperature caused by natural forcings

flux at the TOA in PD relative to PI, which is called transient ERF (TERF). Out of the 10 models mentioned, all the 10 models performed time-slice simulations and can provide aerosol EERF (AEERF), but only six of them performed transient simulations and can provide aerosol TERF (ATERF) (Table 1).

DAMIP (Gillett et al. 2016) performed historical simulations with natural forcings only, anthropogenic greenhouse gases alone, and anthropogenic aerosols alone, facilitating the estimation of climate response (ΔSAT) to individual forcing (experiment id: hist-* in Table 2). All 10 models mentioned above performed transient simulations in DAMIP and can provide aerosol-induced ΔSAT (AΔSAT) (Table 1). The GHGs in RFMIP and DAMIP refer to carbon dioxide (CO_2), methane (CH_4), nitrous oxide (N_2O), and a long list of halocarbons, as described by Meinshausen et al. (2017).

All data were spatially interpolated to a grid resolution of 1° × 1° using bilinear interpolation to enable a meaningful comparison between models (Wang et al. 2021; Xu et al. 2015). For each CMIP6 model, data were obtained from three ensemble members with different initial conditions for each experiment whenever possible, which can reduce the impact of unforced (i.e., internal) variability and enhance the clarity of the signal of interest. This requirement aligns with the experimental protocol (Eyring et al. 2016; Gillett et al. 2016; Pincus et al. 2016). Transient simulations in RFMIP do not follow this requirement. In this study, the results of multimodels are presented by multimodel mean (MMM) ± multimodel standard deviation (MMSD). Prior to calculating MMM, the selected ensemble members are averaged for each model.

The CMIP6 historical anthropogenic emissions of aerosols or aerosol precursors are from the Community Emissions Data System (Hoesly et al. 2018). The datasets provide anthropogenic emissions from eight sectors of activities (agriculture, energy, industrial, transportation, residential–commercial–other, solvent production and application, waste, and international shipping) with a 0.5° horizontal resolution. Gridded versions of these data are accessible through ESGF. Anthropogenic emissions for all species increased significantly in China over the years, as indicated in Table S4 and Fig. S1. The largest increases centered in densely populated city clusters, such as the North China Plain (NCP), the Yangtze River Delta (YRD), the Pearl River Delta (PRD), the Sichuan basin (SCB), and the Fenwei Plain (FWP), all located in eastern China (EC; 18°–44°N, 103°–122°E) (Figs. S2 and S3).

b. *Observational data*

The monthly level-3 (MOD08_M3) Moderate Resolution Imaging Spectroradiometer (MODIS; Remer et al. 2005) AOD product, collected from the *Terra* platform, was used in this study. The AOD data, from February 2000 to December 2014, were retrieved at 550 nm with a horizontal resolution of 1° longitude × 1° latitude.

The observational station data of monthly SAT from 1850 to 2014 in China were acquired from the Climatic Research Unit Temperature version 5 (CRUTEM5; Osborn et al. 2021). Stations that provided data for all 12 months per year were selected to calculate the annual mean SAT. The historical changes in observed SAT and the number of available stations are presented in Fig. S4. Prior to

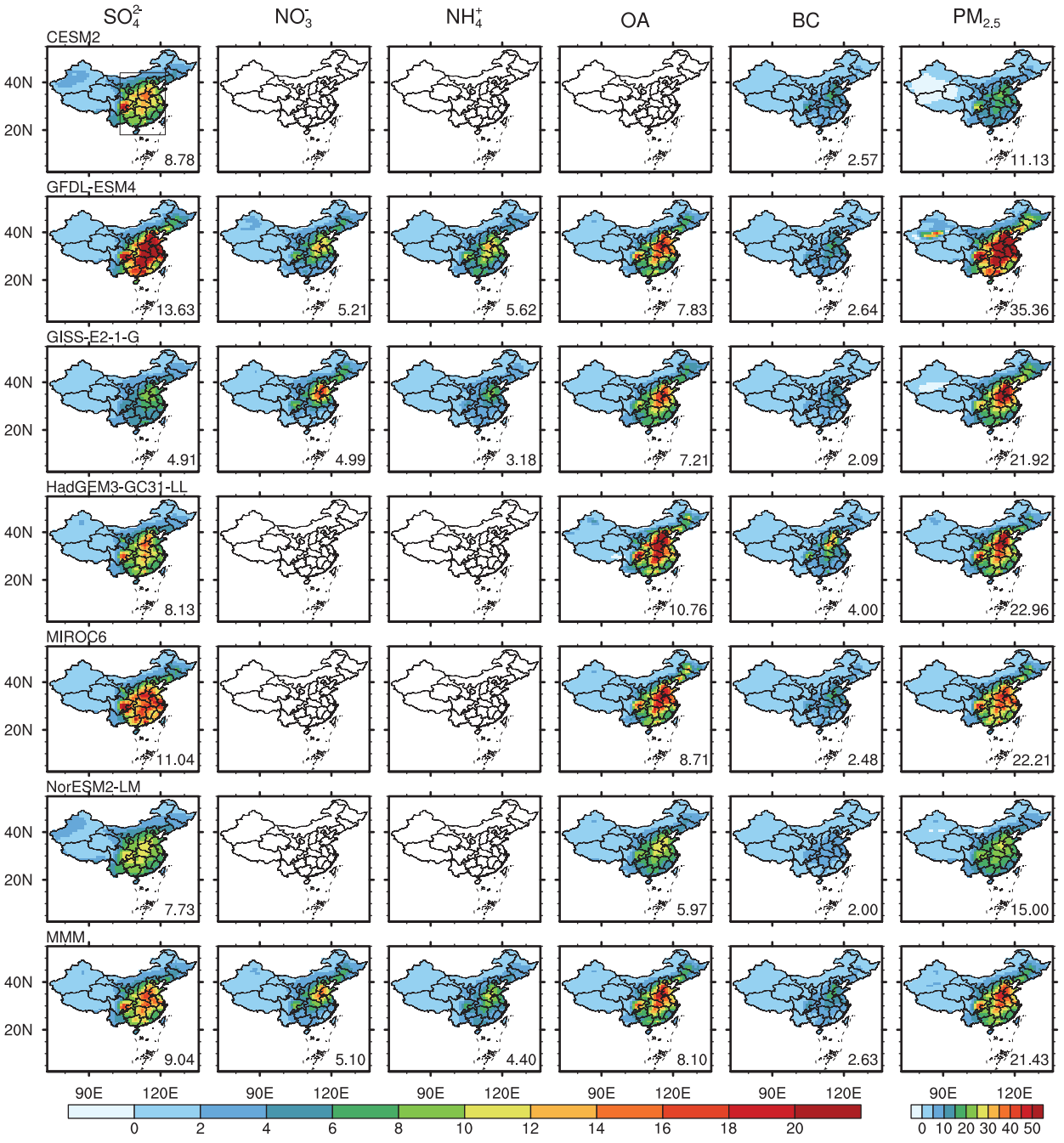

FIG. 2. Spatial distributions of the changes in annual mean surface-layer concentrations of AERs in PD (11-yr mean of 2004–14) relative to the PI period (11-yr mean of 1850–60) from six CMIP6 models (μg m^{-3}). Species here include SO_4^{2-}, NO_3^-, NH_4^+, OA, BC, and $PM_{2.5}$. Concentration of $PM_{2.5}$ was calculated by $PM_{2.5} = SO_4^{2-} + NO_3^- + NH_4^+ + OA + BC + 0.1 \times DU + 0.25 \times SS$. The blank plot indicates that this model has no output for this AER species variable. MMM is the mean of the models that provide data for each species. The rectangle in the top-left plot defines the region of EC (18°–44°N, 103°–122°E). The change averaged over EC is shown in each plot's bottom-right corner. Results from the significance test are not shown in this figure because almost all the grid cells over China have statistically significant changes at $p < 0.05$.

approximately 1950, the national mean temperature exhibited fluctuations due to limited station coverage and uneven distribution. However, after 1950, as monitoring efforts improved, a general upward trend in temperature was observed. To facilitate comparisons with simulated temperatures, the observed temperatures were interpolated to 1° × 1° grids by the Cressman interpolation method.

c. D&A method

In this study, we conducted a detection and attribution analysis on the changes in SAT by employing the three-signal optimal fingerprinting method to separate the individual influence of each external forcing on SAT during 1950–2014. The observed SAT change from CRUTEM5 was regressed onto the modeled SAT responses to GHGs, aerosols (AERs), and natural (NAT) forcings using the least squares algorithm. The regression equation is given by $Y = \beta_{GHG} \times X_{GHG} + \beta_{AER} \times X_{AER} + \beta_{NAT} \times X_{NAT} + \varepsilon$. The term Y is the observed SAT change from CRUTEM5. The term X is the fingerprint that represents the response to individual external forcing (GHG, AER, and NAT) obtained from CMIP6 multimodel means. The regression coefficients β are the scaling factors that adjust the fingerprint values to yield the best match to the observations. When β lies above zero, the corresponding signal is detected. If β is close to unity, it suggests that the simulated responses to the corresponding forcing are in agreement with the observed changes. A scaling factor that is greater (or less) than unity demonstrates underestimation (or overestimation) of the signal to a specific forcing by the models. The term ε is the unforced (internal) variability in SAT, which can be estimated by using unforced preindustrial control simulations from CMIP6 models.

We performed the optimal fingerprinting analyses on the changes in SAT in five typical city clusters (NCP, YRD, PRD, SCB, and FWP) and eastern China as shown in Fig. S3. The regional averages for these areas were calculated for both observed and modeled SATs from 1950 to 2014. The original 65-yr chunk was then transformed into 13 nonoverlapping 5-yr means from 1950–54 to 2010–14 and fed into the regression model. For the internal variability ε, a total number of 155 nonoverlapping 65-yr chunks for SAT were extracted from the available preindustrial control simulations of 10 CMIP6 models (Table S3). For each chunk, ε was averaged in the same way as Y and X, transforming the 65-yr time series into 13 nonoverlapping 5-yr means. To avoid spurious detections, these chunks were divided into two sets. The mean of one set (78 chunks) was used to ascertain the internal variability to obtain the best estimates of β in the regression equation. The mean of the other set (77 chunks) is used to conduct a residual consistency test to check whether the estimated regression residuals fit with modeled internal variability using an F test. The attributable trend of SAT for each external forcing was calculated as the linear trend of the external forcing multiplied by the corresponding scaling factor. The premise of attribution analysis is that the scaling factor in detection analysis is greater than 0.

d. CSA

CSA, the amount of aerosol-induced change in air temperature per unit aerosol ERF, is a widely used measure to quantify the relationship between aerosol forcing and its resulting impact on air temperature (Liu and Liao 2017; Shindell 2014; Shindell and Faluvegi 2009; Shindell et al. 2015). CSA was calculated as slope [°C $(W\ m^{-2})^{-1}$] of the linear regression that passes the origin of the scatterplot

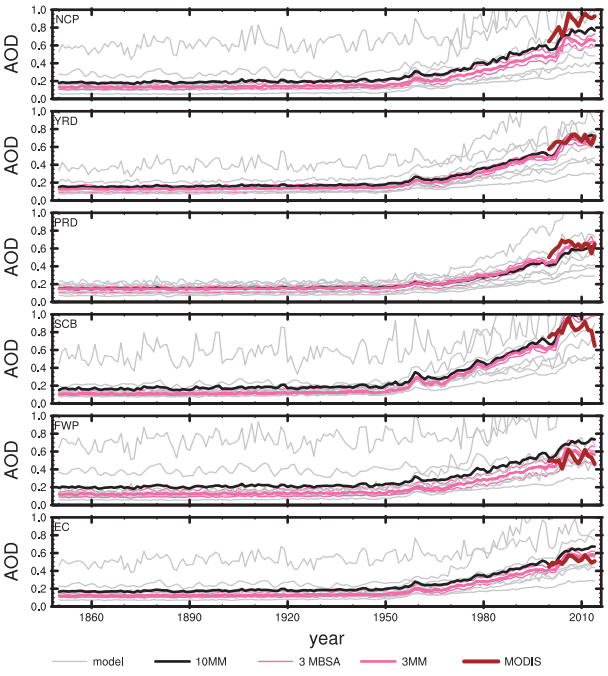

FIG. 3. Time series of annual mean AOD averaged over five typical city clusters (NCP, YRD, PRD, SCB, and FWP) and EC (18°–44°N, 103°–122°E) over 1850–2014 from CMIP6 models (gray line). The black line is 10 MM, and the brown line is MODIS over 2000–14. Three models with better simulations of AOD are shown by pink, and the thicker one is the mean of them (3 MM).

of aerosol-induced ΔSAT (y axis) versus aerosol ERF (x axis) from each of the multimodels. Using the aerosol ERF from equilibrium and transient simulations, we can obtain equilibrium and transient climate sensitivity to aerosols, respectively.

When calculating equilibrium climate sensitivity, the difference between equilibrium and transient responses needs to be considered. Considering the historical simulations can provide the transient AΔSAT, the equilibrium AΔSAT can be calculated for each grid as equilibrium AΔSAT = transient AΔSAT × ΔSAT (piClim-aer − piClim-control)/ΔSAT (piClim-histaer), following Shindell and Faluvegi (2009).

Based on this, this study utilizes linear regression on the AEERF and equilibrium AΔSAT from the 10 models to obtain the equilibrium CSA (ECSA) and linear regression on the ATERF and AΔSAT from the six models to obtain the transient CSA (TCSA). The spatial distribution of CSA is derived by fitting aerosol ERF and AΔSAT at each grid point. When calculating the CSA for the entire EC, the regional means of aerosol ERF and AΔSAT are first calculated, followed by linear regression to determine the CSA for the region.

e. Observational constraint

Using the statistical linear correlation between the uncertain aspect of climate change [usually unobservable, so-called

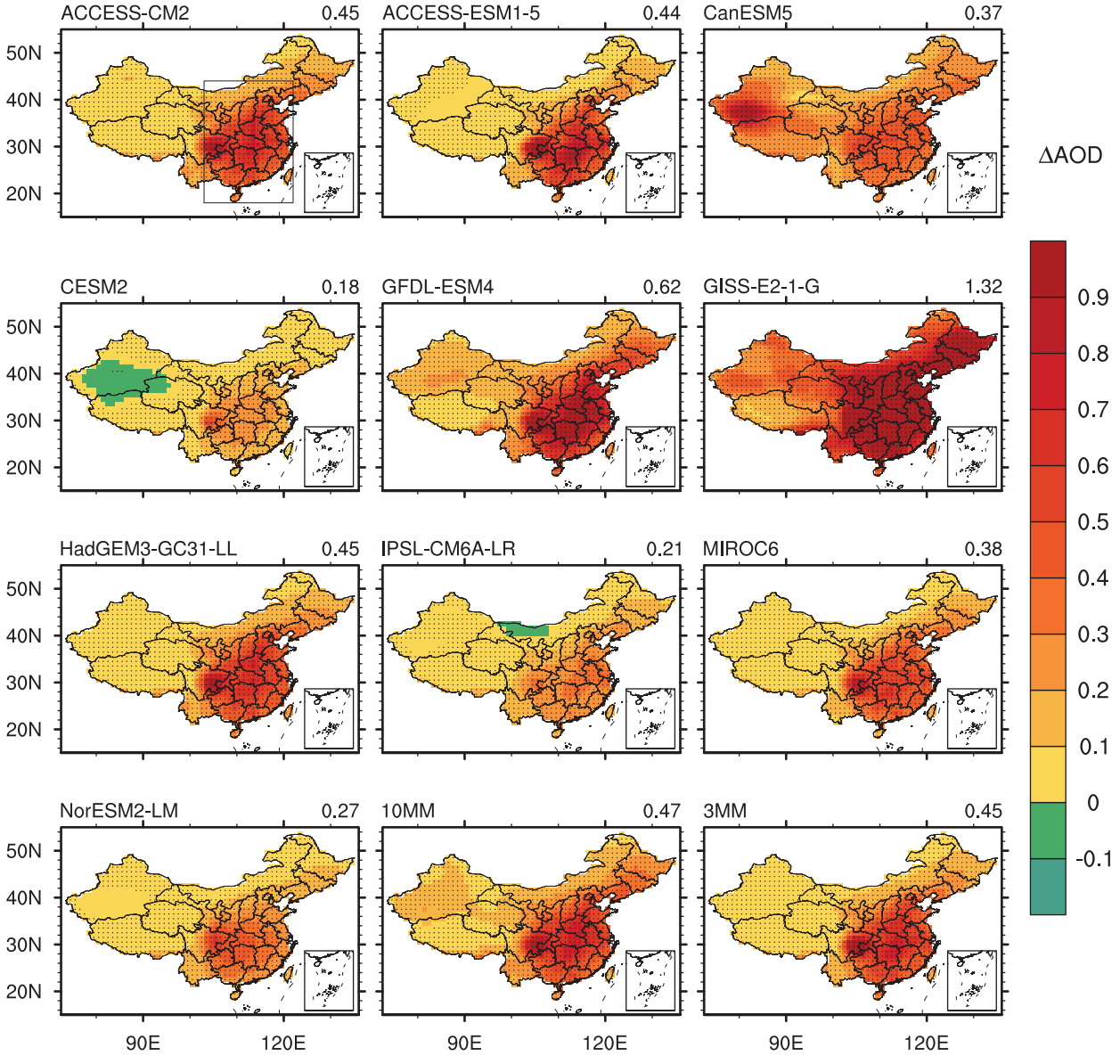

FIG. 4. Spatial distributions of the changes in annual mean AOD in PD (11-yr mean of 2004–14) relative to the PI period (11-yr mean of 1850–60) from 10 CMIP6 models and 10 MM. The mean of three models with better simulations of AOD is also shown (3 MM). The change averaged over EC (18°–44°N, 103°–122°E; the rectangle in the first plot) is shown at the top right of each plot. For each grid, statistically significant change at $p < 0.05$ is marked with dot.

unobservable variable (UBV)] and an observable characteristic known as the constraint factor (CF) in the current climate from multimodels makes it possible to use contemporary observation of CF to constrain UBV (Liu et al. 2022; Watson-Parris et al. 2020). As shown in Fig. S5a, initially, the linear equation that best fits the relationship between UBV Y_1 and CF X was calculated using multimodel results. Subsequently, the observed CF X_O value was inserted into the equation to derive the constrained UBV adj_Y_1. If UBV and CF exhibit a positive correlation, a low bias in multimodel-mean CF compared to its observation would lead to an underestimation of UBV. Using the relationship between two UBVs Y_1 and Y_2, one of which has previously been constrained adj_Y_1, the constrained value of another UBV adj_Y_1 can be obtained (Fig. S5b).

In this study, AOD (mean of 2000–14) can be used as X, and AOD (mean of 2000–14) from MODIS is X_O. SAT (mean of 1950–2014) can also be used as another X, and SAT from CRUTEM5 is another X_O. The variables of the aerosol climate effect that we need to constrain, AEERF, ATERF, and AΔSAT, can be used as Y_1 and directly constrained by the X_O, or they can be used as Y_2 and indirectly constrained by the X_O through a transition variable Y_1. The determination of the constrained variables and processes is presented

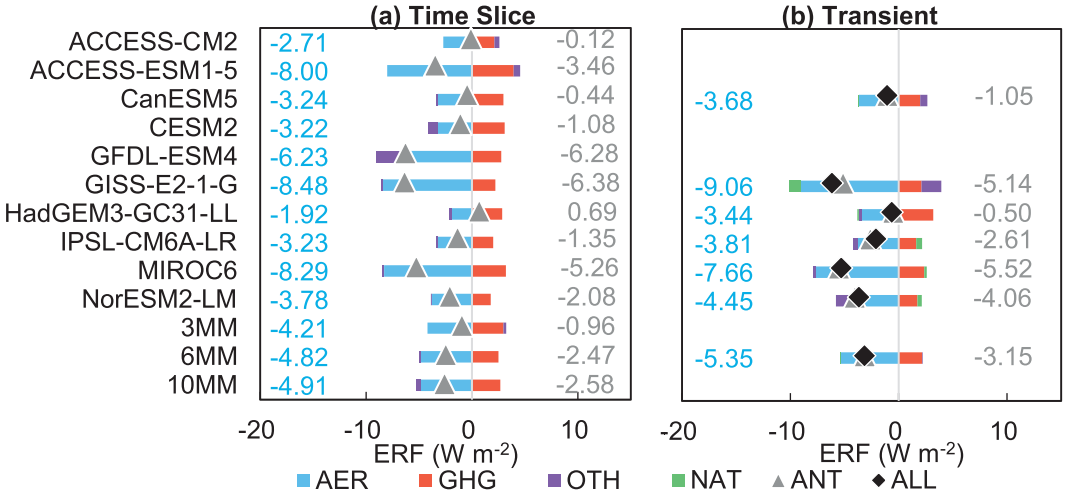

FIG. 5. ERF averaged over EC (18°–44°N, 103°–122°E) from (a) time-slice simulations in 2014 relative to 1850 (10 models) and (b) transient simulations in PD relative to PI (six models). ALL forcings (black) were divided into NAT forcings (green) and ANT forcings (gray). ANT is further divided into AERs (blue), GHGs (red), and OTH (purple). The values of ERF by AER and ANT are also shown. The mean of all 10 models (10 MM), the mean of the six models that performed both time-slice and transient simulations (6 MM), and the mean of three models with better simulations of AOD (3 MM) are also shown.

in section 3e. After obtaining the constrained AEERF, ATERF, and constrained AΔSAT, the constrained climate sensitivity is calculated as the constrained AΔSAT divided by the constrained aerosol ERF. It should be noted that when calculating the constrained ECSA, the ratio mentioned in section 2d should also be considered to correct the constrained AΔSAT. When calculating the CSA in EC, the ERF and AΔSAT averaged over EC should be used for the calculation.

3. Results

a. *Historical change in concentrations of aerosols and AOD*

The simulated changes in annual mean surface-layer concentrations of aerosols in PD relative to PI from CMIP6 models are shown in Fig. 2. The concentration of $PM_{2.5}$ was calculated by the equation $PM_{2.5} = SO_4^{2-} + NO_3^- + NH_4^+ + OA + BC + 0.1 \times DU + 0.25 \times SS$. There were differences in concentrations of $PM_{2.5}$ between the models due to the different aerosol mechanisms. CESM2 simulated the lowest $\Delta PM_{2.5}$ among all models (11.13 $\mu g\ m^{-3}$) because it provided the fewest types of aerosol concentrations (SO_4^{2-} and BC only). GFDL-ESM4 and GISS-E2-1-G are the only two models that include NH_4^+ and NO_3^- (i.e., they include all major aerosol species), and GFDL-ESM4 simulated the highest $\Delta PM_{2.5}$ (35.36 $\mu g\ m^{-3}$). CMIP6 models simulated an increase in annual mean surface $PM_{2.5}$ concentrations over EC of 21.43 ± 7.58 $\mu g\ m^{-3}$ (6 MM ± 6 MSD) from PI to PD. The historical increases in surface aerosols over eastern China were primarily driven by the large increases in anthropogenic emissions of aerosols and aerosol precursors over the PI–PD period. The simulated largest changes in $PM_{2.5}$ concentrations were located in SCB and NCP, consistent with the largest increases in anthropogenic emissions (Fig. S2). As for aerosol components, OA and SO_4^{2-} were simulated to have the largest changes of exceeding 12 $\mu g\ m^{-3}$ (MMM) over the SCB and NCP. BC was the species with the lowest increases in all models, with the 6 MM (±6 MSD) value of 2.63 (±0.66) $\mu g\ m^{-3}$ in EC.

Estimation of climate effect of air pollutants relies not only on surface-layer concentrations but also on column burdens. Figure 3 shows the time series of annual mean AOD averaged over five city clusters (NCP, YRD, PRD, SCB, and FWP) and EC from CMIP6 models, compared with the satellite retrievals from MODIS. In all regions, simulated AOD (10 MM) had small changes from 1850 to around 1950 and then increased sharply when anthropogenic emissions increased markedly, and the increase over SCB was the most pronounced. From around 2010, the increasing trend of AOD in each region tends to be flat or even decline. The model satisfactorily captures this trend of changes but with larger magnitude. From 2000 to 2014, the annual mean AOD averaged over EC increased by 0.20 ± 0.17 from the model (10 MM ± 10 MSD) and by 0.06 from MODIS. The simulated AOD of CMIP6 (10 MM) was higher than the MODIS observation for each year from 2000 to 2014 (except for 2001). The main reason is that the high AOD area from the models is larger than that from the observation (Fig. S6). As shown in Fig. 3, simulated regional mean AOD values were close to observations in YRD and PRD, but they had high biases in SCB and FWP and large low biases in NCP. The same underestimation of AOD in NCP was also reported in other studies (Dang and Liao 2019; Li et al. 2016). Qi et al. (2013) found that MODIS retrievals in northern China tended to show higher AOD values than those obtained from AERONET sites. Various factors including local anthropogenic emissions, chemistry schemes, and model resolution collectively contribute to the uncertainties associated with AOD in climate models (Chang et al. 2015).

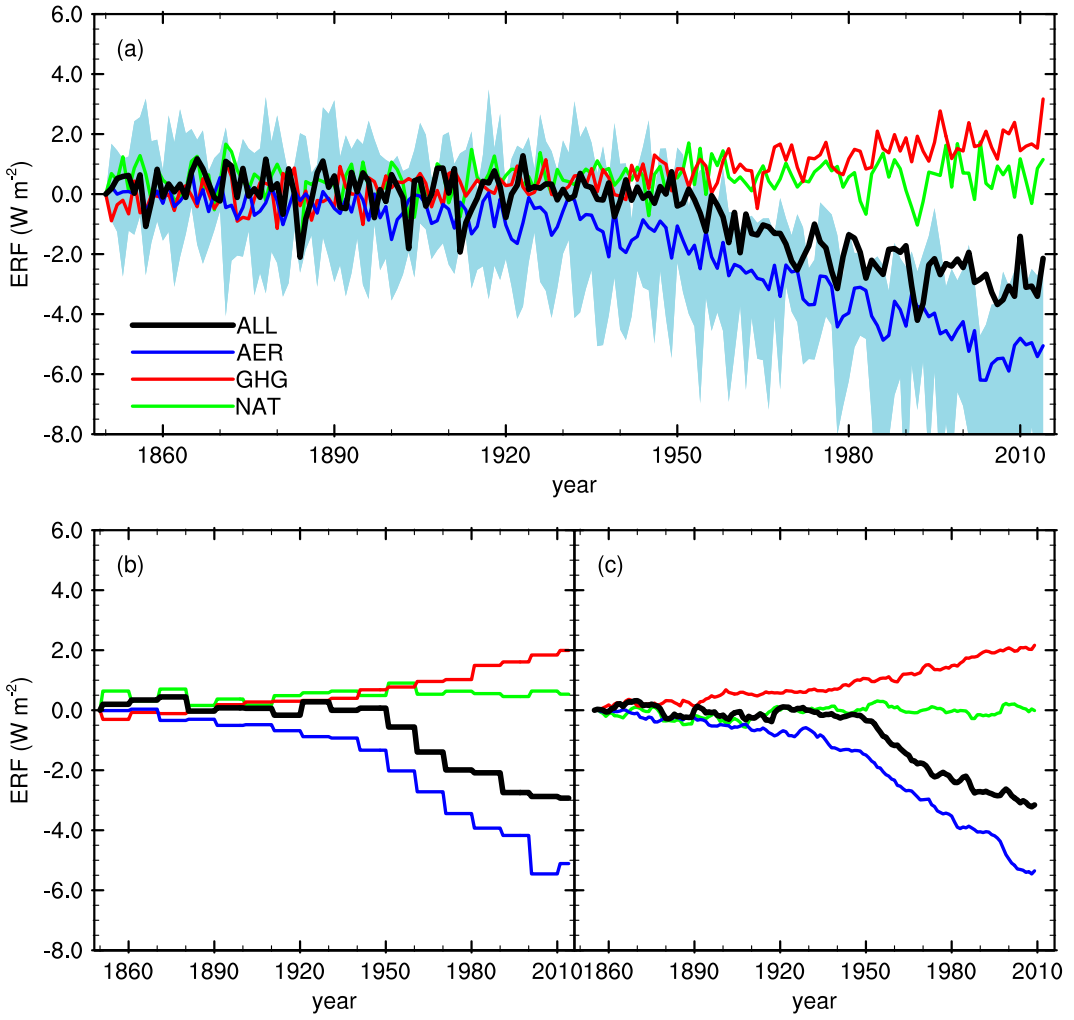

FIG. 6. Six MM ERF by ALL forcings (black line), AERs (blue line), GHGs (red line), and NAT forcings (green line), averaged over EC (18°–44°N, 103°–122°E) from transient simulations over the period of 1850–2014. (a) Annual mean, (b) mean of each decade, and (c) sliding 11-yr mean. The light blue shaded area in plot (a) shows the spread of the six models' data (from minimum to maximum) of AERF.

Spatial correlation coefficients R between each of the 10 CMIP6 models and MODIS were in the range of 0.06–0.84, while the R between 10 MM and MODIS was 0.79 (Fig. S6), indicating that multimodel mean can improve the biases of single models. Three models (ACCESS-CM2, ACCESS-ESM1-5, and HadGEM3-GC3.1-LL) had better simulations of AOD (MBSA), which meet the selected thresholds of $R > 0.75$ and the absolute value of normalized mean bias (NMB) $< 15\%$. The time series of annual mean AOD averaged over five typical city clusters and eastern China from these three MBSAs is also shown in Fig. 3. The three-model-mean (3 MM) AODs were lower than 10 MM AODs from 1850 to 2014, and the values in 2000–14 were closer to MODIS values, but still underestimated in NCP (Fig. 3). Historically, all models simulated the increases in AOD in most regions of China, with the increases being higher in EC and lower in western China, consistent with the spatial distribution of historical increases in aerosol concentrations (Fig. 4). The largest simulated ΔAOD occurs in SCB. From PI to PD, the increase in AOD in EC was 0.47 ± 0.33 (10 MM ± 10 MSD). As for the three MBSAs, the ΔAOD in EC was 0.45 ± 0.01 (3 MM ± 3 MSD), with smaller uncertainty range.

b. *Aerosol ERF*

Figure 5a shows the ERFs from RFMIP multimodel time-slice simulations that are averaged over EC (18°–44°N, 103°–122°E). Anthropogenic (ANT) drivers include GHGs (including CO_2, CH_4, N_2O, and a long list of halocarbons), AERs, and others (OTH). From 1850 to 2014, the increases in aerosols led to a negative equilibrium ERF of -4.91 ± 2.56 W m^{-2} (10 MM ± 10 MSD) over EC, which agrees closely with aerosol ERF in 2005 (-4.14 W m^{-2}) in eastern China (20°–45°N, 105°–122°E) obtained by Liu and Liao (2017) using phase 5 of the CMIP (CMIP5) multimodel results. The negative ERF in this study

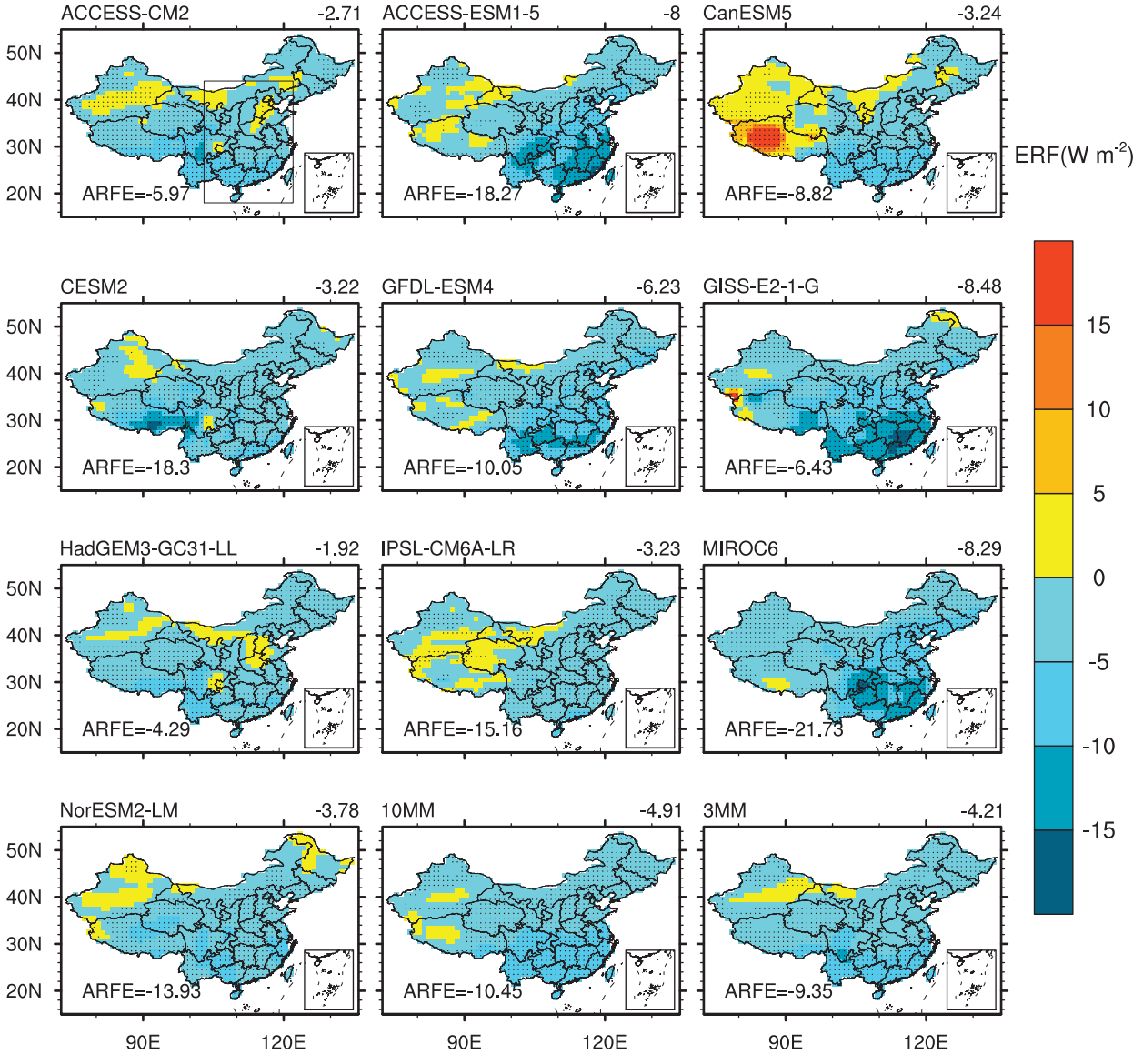

FIG. 7. Spatial distributions of simulated annual mean AEERF in 2014 relative to 1850 from time-slice simulations of 10 CMIP6 models and 10 MM. The ERF averaged over EC (18°–44°N, 103°–122°E; the rectangle in the first plot) is shown at the top right of each panel. For each grid, statistically significant change at $p < 0.05$ is marked with dot. The mean of three models with better simulations of AOD is also shown (3 MM). The bottom-left corner of each plot shows every model's ARFE (AER radiative forcing per unit AOD change).

is higher, which can be partly explained by the higher AOD in 2014 relative to 2005. The absolute value of negative ERF of 3 MM is smaller than that of 10 MM, which is consistent with the smaller ΔAOD in 3 MM. Over EC, the absolute value of negative ERF caused by the increases in aerosols was larger than that of the positive ERF brought by the increases in GHGs, leading to a net negative ERF by anthropogenic drivers.

Transient simulations provide transient ERF (Fig. 5b) of all (ALL) forcings, which can be divided into ANT and NAT. Only six models conducted transient simulations. From PI to PD, aerosol transient ERF over EC was -5.35 ± 2.40 W m^{-2} (6 MM ± 6 MSD). Aerosol transient ERF was bigger than its equilibrium ERF in all of the six models except for MIROC6. Figure S7 shows the aerosol DRF (the aerosol-induced change in radiative flux under clear-sky condition) and cloud radiative forcing (CRF; the difference between ERF and DRF) (Rotstayn and Penner 2001) averaged over eastern China from equilibrium and transient simulations. Only five models have both equilibrium and transient DRF and CRF values. The means of these five models show that the equilibrium and transient DRF values are -5.85 and -5.87 W m^{-2}, respectively; the equilibrium and transient CRF values are 0.45 and 0.14 W m^{-2}, respectively, and the equilibrium and

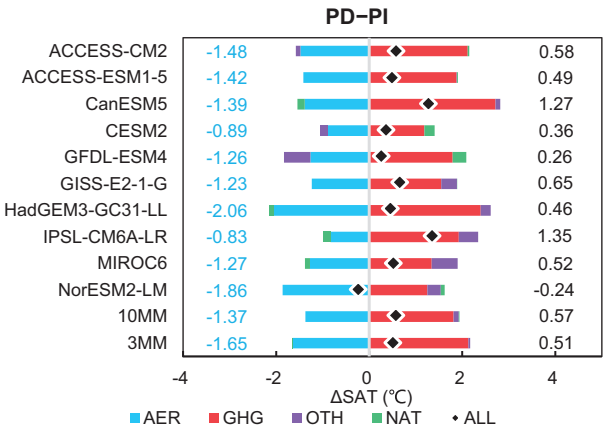

FIG. 8. Change in simulated annual mean SAT from 10 models averaged over EC (18°–44°N, 103°–122°E) in PD relative to PI by different forcings. ALL forcings (black) were divided into NAT forcings (green) and ANT forcings which is further divided into AERs (blue), GHGs (red), and OTH (purple). The mean of all 10 models (10 MM) and the mean of three models with better simulations of AOD (3 MM) are also shown.

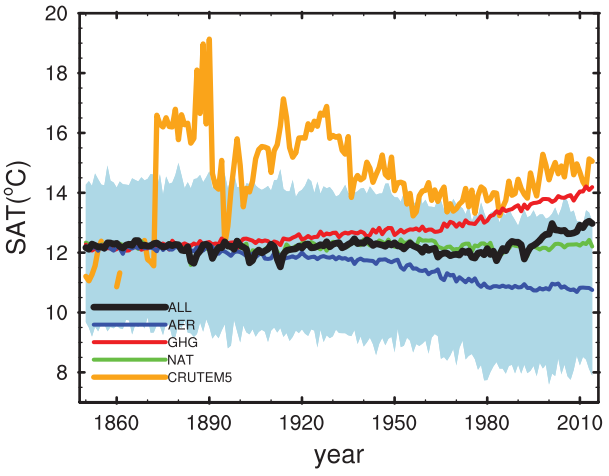

FIG. 9. Time series of annual mean SAT averaged over EC (18°–44°N, 103°–122°E) of 10 CMIP6 models from four experiments: historical (ALL; black line), hist-aer (AER; blue line), hist-GHG (GHG; red line), and hist-nat (NAT; green line). The observational data from CRUTEM5 are also shown (orange line). The light blue shaded area shows the spread of the 10 CMIP6 models' data in hist-aer.

transient ERF values are −5.40 and −5.73 W m^{-2}, respectively. Therefore, the transient ERF is larger than the equilibrium forcing because of the smaller positive CRF in the transient simulations.

Same as equilibrium ERF, the negative ERF caused by the increases in aerosols was larger than the positive ERF from the increases in GHGs, leading to a net negative ERF by ANT and further a net negative ERF by all forcings, with practically zero contributions from NAT or OTH. Transient simulations also provide a complete time series of ERFs from 1850 to 2014 (Fig. 6). ERF by all forcings (black lines in Fig. 6) was almost unchanged until 1950, after which it began to show negative values. This was mainly due to the negative ERF by aerosols, although it was partly offset by positive ERF by greenhouse gases. Unlike the global turning point in about 1980 (Smith et al. 2021), the turning point for China was around 2000, after which the negative aerosol ERF weakened slightly.

Figure 7 shows the spatial distributions of simulated present-day annual mean equilibrium ERF by aerosols (year 2014 relative to 1850) from time-slice simulations. The geographical distribution of aerosol ERF shows higher negative values of −5 to −20 W m^{-2} over the southern China. Aerosol ERF varies greatly among the models, in terms of both magnitude and spatial distribution. The largest negative aerosol ERF values were simulated in southeastern China in ACCESS-ESM1-5 and GISS-E2-1-G; in southwestern China in ACCESS-CM2, CESM2, HadGEM3-GC3.1-LL, NorESM2-LM, and MIROC6; and in the whole southern China in CanESM5, GFDL-ESM4, and IPSL-CM6A-LR. Some models showed positive aerosol ERF values in certain regions, such as northern China and western China, likely due to the high surface albedo enhancing the effect of absorbing aerosols (Schulz et al. 2006). Moreover, the positive ERF values could also be linked to the changes in clouds and longwave radiation resulting from the quick adjustment of the atmosphere (Wang et al. 2014). The spatial distributions of aerosol transient ERF were about the same as those of aerosol equilibrium ERF in most models (Fig. S8).

Although the aerosol indirect effect is considered in all the CMIP6 models, the parameterizations of aerosol–cloud interactions are quite different. Figure 7 also presents aerosol radiative forcing efficiency (ARFE), defined as aerosol radiative forcing per unit AOD change or aerosol burden change (Kasoar et al. 2016; Myhre et al. 2013b; Samset et al. 2013). Over EC, ARFE (ERF averaged over EC divided by ΔAOD averaged over EC) values were in the range of −4.29 W m^{-2} in HadGEM3-GC3.1-LL to −21.73 W m^{-2} in MIROC6. Considering the three MBSAs, ACCESS-ESM1-5 had the smallest ΔAOD of 0.44, whereas the largest aerosol ERF was −8 W m^{-2}; thus, its ARFE (−18.27 W m^{-2} per unit AOD change) was the largest among the three models. When we use aerosol transient ERFs to calculate ARFE, the results are slightly larger than using equilibrium ERFs, as a result of the larger transient ERF with the same ΔAOD in each model (except MIROC6) (Fig. S8). There are many reasons for the differences in ARFE, such as radiative transfer schemes, surface albedo, cloud interactions, and other different properties in different models (Kasoar et al. 2016; Myhre et al. 2013b; Randles et al. 2013; Stier et al. 2013).

c. *Aerosol-induced change in SAT*

From PI to PD, simulated changes in annual mean SAT averaged over EC were warming in almost all 10 CMIP6 models (except for NorESM2-LM), with the 10 MM (±10 MSD) value of +0.57 (±0.46)°C, in which GHGs caused an increase of 1.81 (±0.5)°C and aerosols caused a decrease of

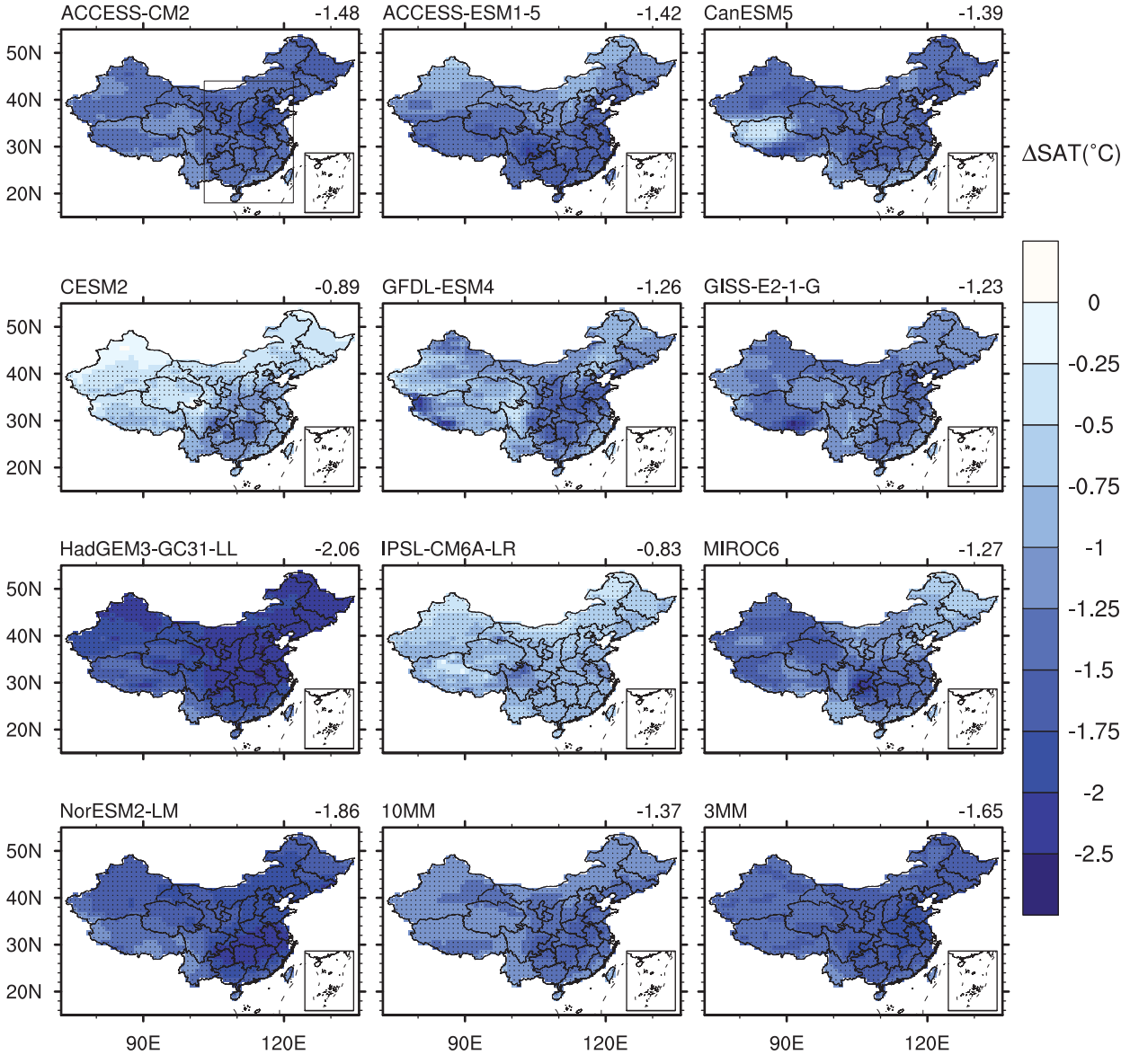

FIG. 10. Spatial distributions of AER-induced change in simulated annual mean SAT in PD (11-yr mean of 2004–14) relative to the PI period (11-yr mean of 1850–60) of 10 CMIP6 models and 10 MM in the simulation hist-aer. The change averaged over EC (18°–44°N, 103°–122°E; the rectangle in the first plot) is shown at the top right of each plot. For each grid, statistically significant change at $p < 0.05$ is marked with dot. The mean of three models with better simulations of AOD is also shown (3 MM).

1.37 (±0.38)°C (Fig. 8). The aerosol-induced air temperature decrease of −1.37°C in this study is slightly larger than the −1.05°C obtained by Liu and Liao (2017) using the CMIP5 multimodel results, which is consistent with the previous comparison of ERF (−4.91 W m^{-2} from this work vs −4.14 W m^{-2} in Liu and Liao 2017). Simulations from the 3 MBSAs (3 MM) obtained a larger aerosol cooling of −1.65°C over EC.

Figure 9 shows the time series of annual mean SAT (10 MM) averaged over EC from four experiments: historical, hist-aer, hist-GHG, and hist-nat. The simulated SAT was lower than the observed value from CRUTEM5, because of the underestimation in the central and western ECs, such as the SCB and Hubei Province (Fig. S9). Over 1920–80, aerosols and greenhouse gases had pronounced effects on SAT, with a similar magnitude but opposite sign relative to 1850. Starting around 1980, the aerosol-induced cooling tended to have a small change (stayed around −1.5°C relative to 1850) and GHG-induced warming kept increasing, which led to an overall warming of about 1°C in 2014 relative to 1850. Figure 9 also shows that the air temperature in hist-nat remained relatively stable from 1850 to 2014.

All the 10 models simulated a national cooling by aerosols, with large cooling in EC (Fig. 10). NCP, SCB, and the Yangtze

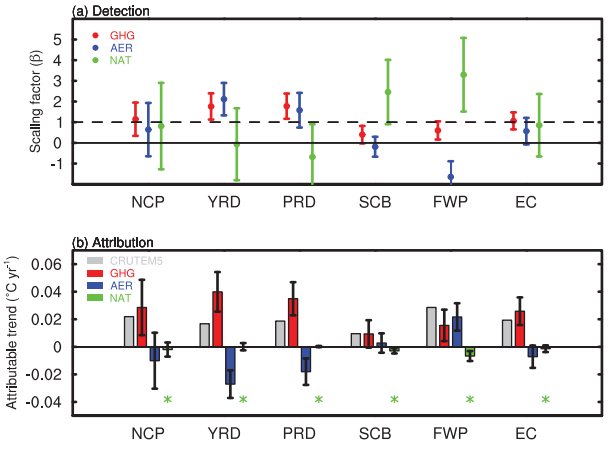

FIG. 11. (a) Detection and (b) attribution of annual mean SAT change over five typical city clusters (NCP, YRD, PRD, SCB, and FWP) and EC from 1950 to 2014. (a) Scaling factors and their 90% confidence intervals for GHG (red), AER (blue), and NAT (green). (b) Attributable trends of SAT (°C yr^{-1}) to GHG (red), AER (blue), and NAT (green) signals compared with the observed trends from CRUTEM5 (gray). An asterisk (*) indicates that the trend is not statistically significant ($p > 0.05$).

River basin were the areas with the largest cooling, which did not agree with the spatial distributions of aerosol ERF in Fig. 7, because the changes in temperature can be affected not only by local ERF but also by energy transport through large-scale atmospheric or oceanic circulations (Shindell et al. 2015; Shindell et al. 2010). The models vary in the spatial distribution of temperature decrease. The simulated cooling effect from the 3 MBSAs (3 MM) was larger than 10 MM, with the largest cooling of −1.75° to −2.0°C in NCP and SCB. Given that ACCESS-CM2 and HadGEM3-GC3.1-LL simulated a similar AOD change and slightly different aerosol ERF, it is surprising that there were large differences in the magnitude of simulated climate response. Averaged over EC, while HadGEM3-GC3.1-LL had the smallest AEERF among all models of −1.92 W m^{-2} and the largest aerosol-induced cooling of 2.06°C, ACCESS-CM2 had an AEERF of −2.71 W m^{-2} and cooling of 1.48°C. The climate response does not follow the magnitude of ERF, which can be explained by the different climate sensitivity in different models (Flato et al. 2013; Voulgarakis and Shindell 2010).

We performed the optimal fingerprint analysis on the changes in SAT over five typical city clusters (NCP, YRD, PRD, SCB, and FWP) and EC (Fig. S3) to quantify the contribution of aerosols to historical climate change more accurately. All regions passed the residual consistency test. The scaling factors are shown in Fig. 11a. AER signals can be detected in NCP, YRD, PRD, and EC, as indicated by the scaling factors that are larger than zero over these regions. SAT responses to AER are relatively well aligned with the observations, as the scaling factors over NCP (β = 0.64), PRD (β = 1.58), and EC (β = 0.57) are close to 1.0. However, β over YRD (2.12) is much higher than 1.0, indicating the considerable underestimation of aerosol-induced SAT change by models. The scaling factors of AER in SCB and FWP are lower than zero. D&A analysis of each grid nationwide (Fig. S10) indicates that the aerosol effect can be detected in most grids in NCP, YRD, and PRD, but can only be detected in small areas of SCB and FWP, such as the border area of the three provinces in FWP and the easternmost part of SCB. The observed and attributable trends of SAT are illustrated in Fig. 11b. The observed warming trends were 0.009°–0.029°C yr^{-1} in the five city clusters and 0.019°C yr^{-1} in EC. Aerosols were found to cause the largest cooling trend in YRD (−0.027°C yr^{-1}), which also offset the maximum percentage (68%) of GHG-induced warming. Aerosol offset GHG-induced warming in the NCP and PRD by 35% and 52%, respectively. Over EC, considering the warming of 0.019°C yr^{-1} from 1950 to 2014, aerosols caused a cooling of 0.007°C yr^{-1}, which offset 28% of the GHG-induced warming (0.026°C yr^{-1}). The trend in SAT caused by NAT was small and insignificant; therefore, the difference between the warming trend caused by GHGs and the observed warming trend was all contributed by aerosols.

d. CSA

CSA was defined as aerosol-induced change in air temperature per unit aerosol ERF. The ECSA was calculated using AEERF and equilibrium AΔSAT from 10 models, and the TCSA were calculated using ATERF and AΔSAT from six models (section 2d). Over EC, ECSA was 0.236°C (W m^{-2})$^{-1}$, which was slightly greater than TCSA of 0.222°C (W m^{-2})$^{-1}$. Our results are in agreement with previous studies. Shindell and Faluvegi (2009) reported that the regional climate response to sulfate aerosol over the latitudinal range of 28°–60°N was about 0.25°C (W m^{-2})$^{-1}$. Liu and Liao (2017) estimated ECSA in eastern China (20°–45°N, 105°–122.5°E) to be 0.24°C (W m^{-2})$^{-1}$ using the multimodel results from CMIP5.

Figure 12 shows the spatial distributions of ECSA and TCSA. Both ECSA and TCSA were obviously lower in southern China [<0.2°C (W m^{-2})$^{-1}$] and higher in northern China [>0.2°C (W m^{-2})$^{-1}$], divided by the Qinling Mountains and the Huaihe River. In some parts of Xinjiang, climate sensitivity was negative; that is, the positive ERF in this area caused decreases in temperature. Local climate sensitivity varied strongly due to the presence of different feedbacks (e.g., snow/ice albedo and ocean circulation) (Shindell et al. 2015). Shindell et al. (2015) also showed that CSA in the Northern Hemisphere extratropic is greater than in the tropics. In the southern coastal region, ECSA is slightly larger than TCSA. In the northern EC, TCSA is slightly larger than ECSA.

e. Observation-constrained aerosol climate effect

As mentioned in section 2e, an UBV can be constrained by the observed CF through the statistical linear correlation of these two variables from multimodel simulations. To constrain the climate effect of aerosols, the variables that need to be constrained include AEERF, ATERF, and AΔSAT. A variable Y_1 can be directly constrained by X_O, or a variable Y_2 can be indirectly constrained by X_O through a transition

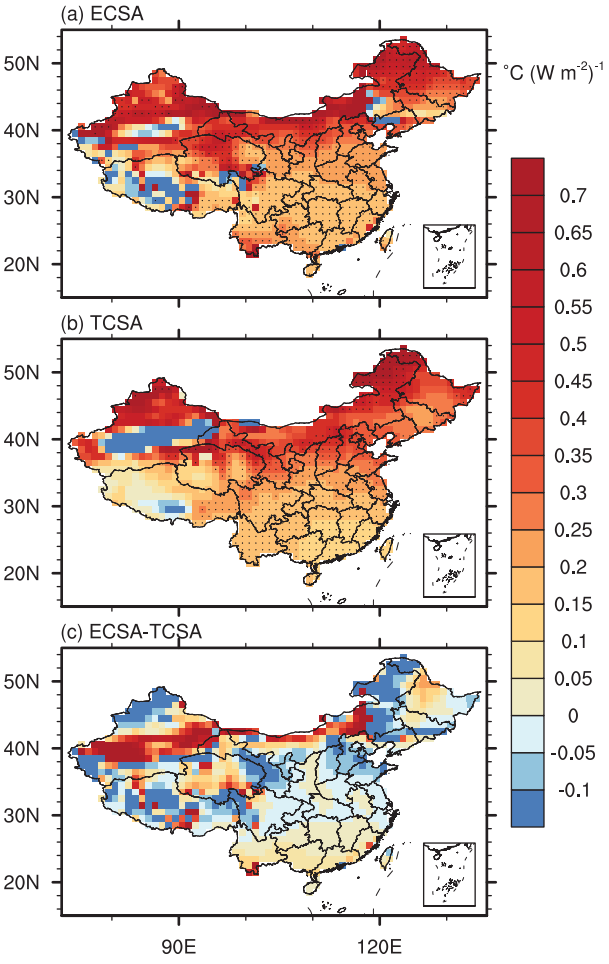

FIG. 12. Spatial distributions of (a) ECSA, (b) TCSA, and (c) the difference between ECSA and TCSA [°C $(W\ m^{-2})^{-1}$]. For each grid, the slope that pass the significance test at $p < 0.05$ is marked with dot.

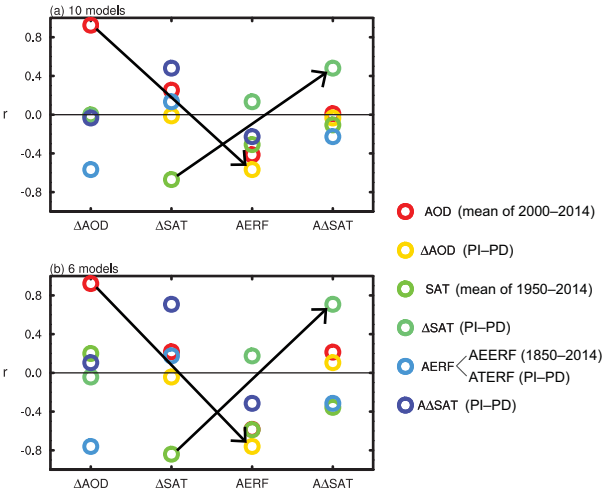

FIG. 13. The correlation coefficients between the variables averaged over EC (18°–44°N, 103°–122°E) from CMIP6 multimodels. The variables are from (a) 10 models and (b) six models. AERF in (a) is the AEERF. AERF in (b) is the ATERF. Arrows represent the processes of constraining, as described in the text. PI indicates the PI time (11-yr mean of 1850–60), and PD indicates the PD (11-yr mean of 2004–14).

variable Y_1, as shown in Fig. S5. The term X_O used in this study is AOD (mean of 2000–14) from MODIS or SAT (mean of 1950–2014) from CRUTEM5.

The values of each variable averaged over EC (18°–44°N, 103°–122°E) were used to calculate the correlation coefficients between each other. We show first the correlation coefficients calculated by using model results from the 10 models which provide values of AEERF and AΔSAT (Fig. 13a). Among all the variables considered, AEERF has the best correlation (determined by the largest absolute value of correlation coefficient) with ΔAOD, so ΔAOD can be used to constrain AEERF. In the meantime, ΔAOD has the best correlation with AOD, indicating AOD_MODIS can be used to constrain ΔAOD to get adj_ΔAOD and subsequently adj_AEERF. Similarly, AΔSAT has the best correlation with ΔSAT, while ΔSAT has the best correlation with SAT, so SAT_CRUTEM5 can be used to constrain ΔSAT to get adj_ΔSAT and subsequently adj_AΔSAT. The black arrows in the figure show these two processes.

The constrained results by using the 10 models are shown in Fig. 14. The observation-constrained AEERF (adj_AEERF) has a similar spatial distribution to AEERF_10MM (Fig. 7) except that the largest negative forcing is now in PRD. Averaged over EC, while AEERF_10MM is $-4.91\ W\ m^{-2}$, adj_AEERF is $-4.66\ W\ m^{-2}$, which is due to the overestimation of AOD by 0.08 and hence the overestimation of ΔAOD by 0.06. The values of adj_AEERF minus AEERF_10MM are positive in most regions such as SCB and FWP, indicating that adj_AEERF has smaller negative forcing in these regions relative to AEERF_10MM. On the contrary, adj_AEERF has larger negative forcing in NCP and PRD relative to AEERF_10MM. The spatial distribution of adj_AEERF minus AEERF_10MM corresponds well to that of adj_ΔAOD minus ΔAOD_10MM for the reasons mentioned above.

The values of adj_AΔSAT minus AΔSAT_10MM were negative nationwide except in the northeastern China, indicating enhanced cooling by aerosols after the constraint as compared to AΔSAT_10MM. The enhanced cooling was the largest in central China. As a result, adj_ECSA had a similar spatial distribution to ECSA, but the values were approximately doubled. In EC, adj_AΔSAT was −1.47°C and adj_ECSA was $0.32°C\ (W\ m^{-2})^{-1}$.

Similarly, considering the six models that provide outputs of ATERF, the same approaches can be obtained as shown in Fig. 13b: 1) using AOD_MODIS to constrain ΔAOD and then using adj_ΔAOD to constrain ATERF; 2) using SAT_CRUTEM5 to constrain ΔSAT and then using adj_ΔSAT to constrain AΔSAT. The climate sensitivity after constraint is calculated as adj_TCSA = adj_AΔSAT/adj_ATERF. It should be noted that adj_ΔAOD, adj_ΔSAT, and adj_AΔSAT involved in this set of constraints were obtained by using the results of six models.

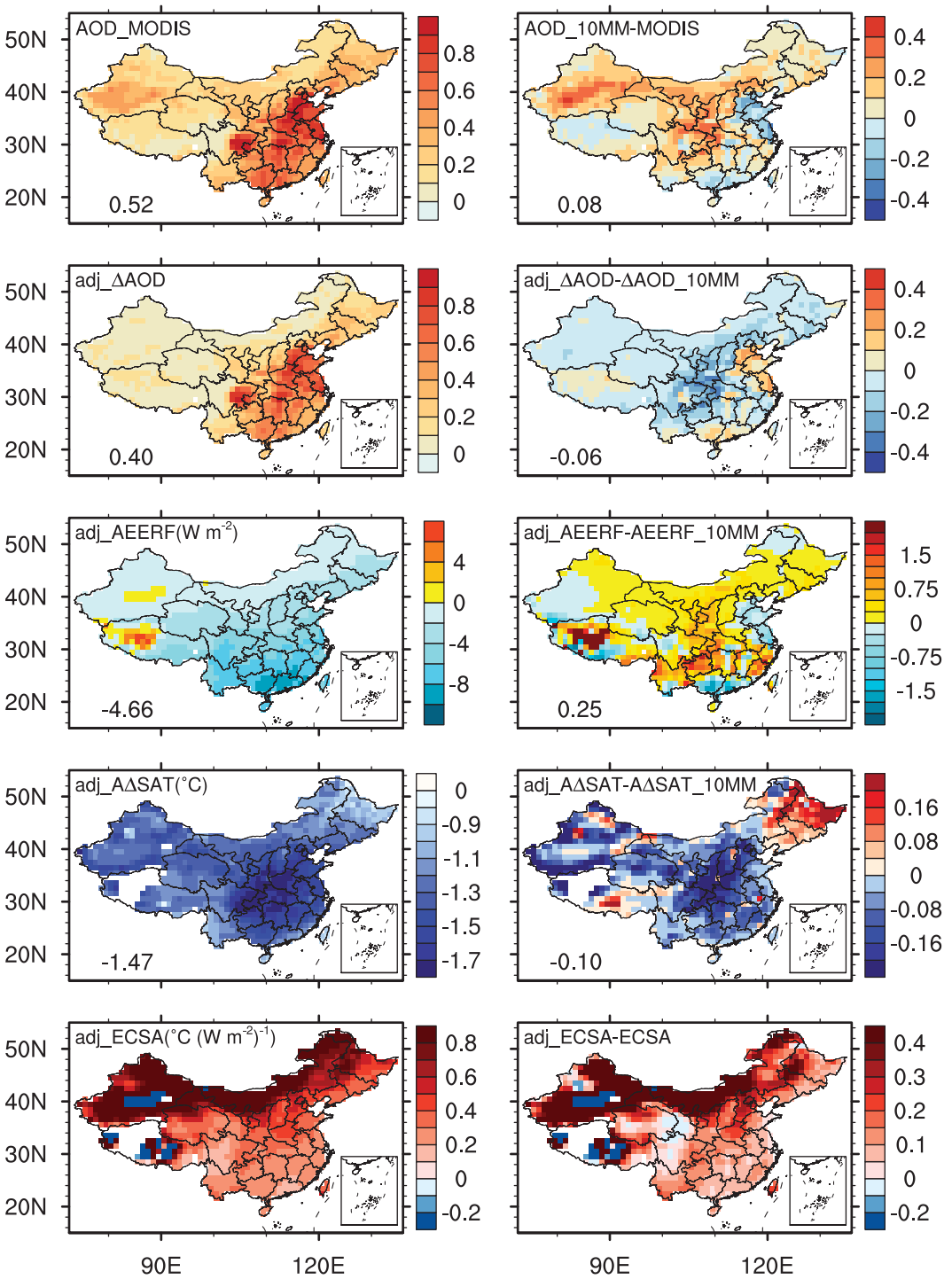

FIG. 14. Observation-constrained results of historical changes in AERs and their climatic effects using 10 models. (left) Observed AOD from MODIS or the constrained values of other variables and (right) the difference between (left) and the respective simulated value (10 MM). The value averaged over EC (18°–44°N, 103°–122°E) is shown in each plot's bottom-left corner.

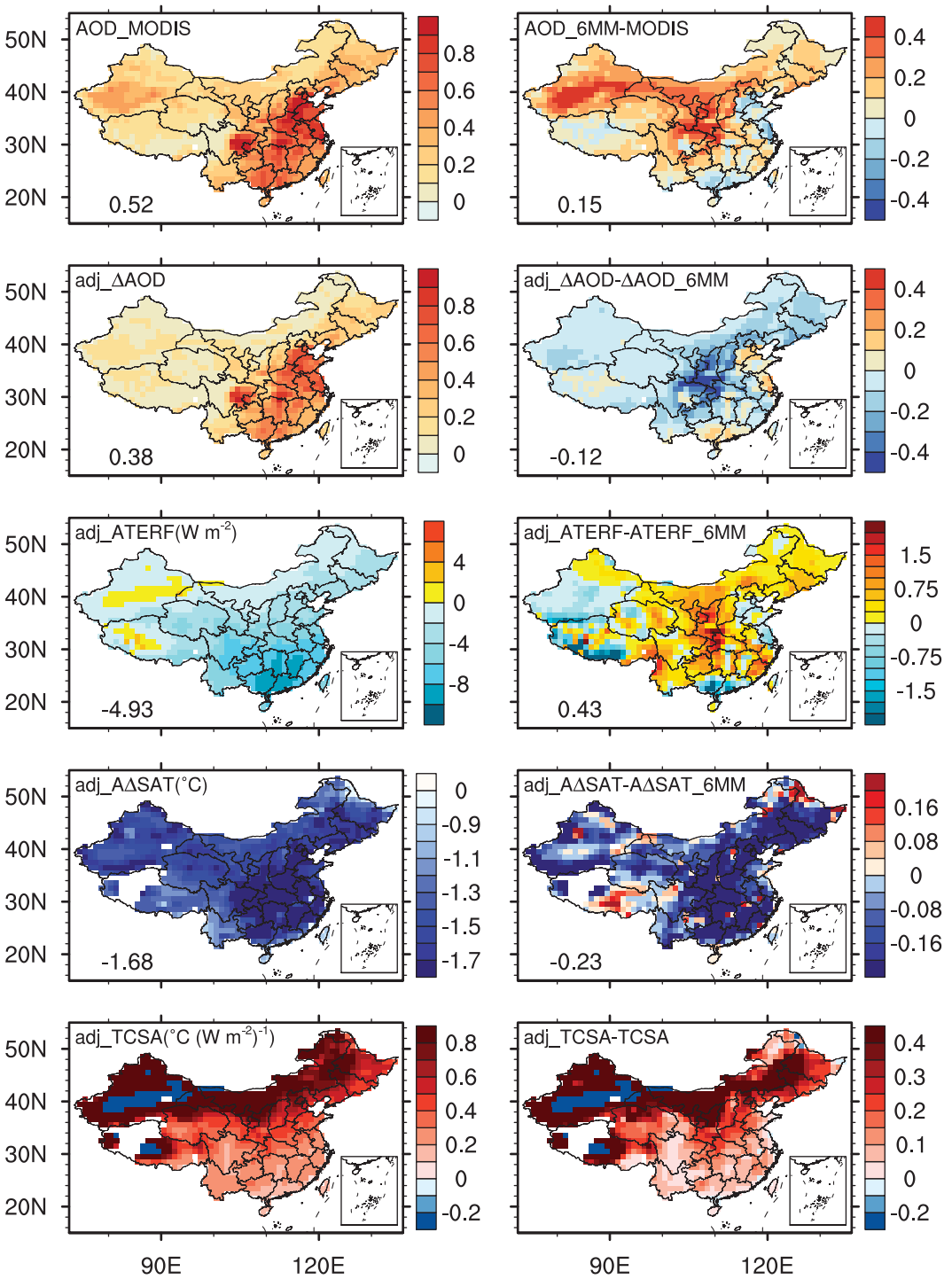

FIG. 15. Observation-constrained results of historical changes in AERs and their climatic effects using six models. (left) Observed AOD from MODIS or the constrained values of variables and (right) the difference between (left) and the respective simulated value (6 MM). The value averaged over EC (18°–44°N, 103°–122°E) is shown in each plot's bottom-left corner.

The constrained results are shown in Fig. 15. The spatial distribution of adj_ATERF is basically the same as that of adj_AEERF, with the highest negative values in PRD. Averaged over EC, adj_ATERF was -4.93 W m^{-2} as compared to the ATERF_6MM of -5.35 W m^{-2}. The spatial distribution of adj_ATERF minus ATERF_6MM is also similar to that of adj_AEERF minus AEERF_10MM. Averaged over EC, adj_AΔSAT was -1.68°C, which was stronger than the AΔSAT_6MM value of -1.44°C. The Adj_TCSA in EC was 0.34°C (W m^{-2})$^{-1}$.

4. Conclusions

This study used the CMIP6 multimodel results to analyze the changes in aerosols since industrialization as well as the associated aerosol ERF and aerosol-induced SAT changes using simulations from RFMIP and DAMIP. Most importantly, we used observations to constrain the modeled ERF, changes in SAT, and climate sensitivity to aerosols. Considering the availability of model outputs, either six-model-mean (6 MM) or 10 MM was analyzed.

Averaged over EC, the simulated annual mean surface $PM_{2.5}$ concentration and AOD increased by 21.43 ± 7.58 μg m^{-3} (6 MM ± 6 MSD) and 0.47 ± 0.33 (10 MM ± 10 MSD), respectively, from PI to PD. The simulated largest increases in AOD occurred in SCB. Compared to observations from MODIS, the CMIP6 models (10 MM) overestimated AOD by 0.08 as the values were averaged over EC and years of 2000–14, which were used to constrain aerosol ERF.

The increases in historical aerosols in EC led to an equilibrium ERF of -4.91 ± 2.56 W m^{-2} (10 MM ± 10 MSD) from time-slice simulations and a transient ERF of -5.35 ± 2.40 W m^{-2} (6 MM ± 6 MSD) from transient simulations. The negative ERF values were generally larger in southern China and smaller in northern China. After the constrain by using observed AOD from MODIS, adj_AEERF and adj_ATERF over EC were -4.66 and -4.93 W m^{-2}, respectively.

The negative aerosol ERF caused nationwide decreases in SAT in China, especially in areas with large increases in AOD such as SCB, but the distribution of ΔSAT was not consistent with that of aerosol ERF, mainly because local temperature changes were not solely related to local radiative flux changes. The time series of ΔSAT exhibited large absolute values starting around 1950 and reached a cooling of 1.37° ± 0.38°C (10 MM ± 10 MSD) by aerosols averaged over EC in PD relative to PI. The CMIP6 models underestimated SAT compared to the observations from CRUTEM5. After the constrain by using SAT from CRUTEM5, adj_AΔSAT was -1.47 W m^{-2} over EC.

The spatial distributions of equilibrium CSA and transient CSA were similar to each other in China, with low CSA in southern China and high CSA in northern China. Over EC, ECSA was 0.236°C (W m^{-2})$^{-1}$ and TCSA was 0.222°C (W m^{-2})$^{-1}$. The adjusted CSA after constraint is calculated by dividing adjusted AΔSAT by adjusted aerosol ERF. The adj_ECSA and adj_TCSA were higher in magnitude but kept a similar spatial distribution. The adj_ECSA and adj_TCSA in EC were 0.32° and 0.34°C (W m^{-2})$^{-1}$, respectively.

Our study constrained aerosol ERF using only the observed AOD. Further studies should also consider aerosol single scattering albedo for the constraint of absorbing aerosols. Moreover, we will use observations to constrain the predicted future climatic effects of aerosols.

Acknowledgments. This study was supported by the National Key Research and Development Program of China (Grant 2019YFA0606800).

Data availability statement. CMIP6 dataset was accessed at ESGF (https://esgf-node.llnl.gov/search/cmip6/). Gridded dataset of the historical anthropogenic emissions was accessed through ESGF (https://esgf-node.llnl.gov/search/input4mips/) under the institution = "PNNL-JGCRI." MODIS AOD data are available at https://giovanni.gsfc.nasa.gov/giovanni/. CRUTEM5 historical observed surface air temperatures are available at https://www.metoffice.gov.uk/hadobs/crutem5/.

REFERENCES

Allen, M. R., and S. F. B. Tett, 1999: Checking for model consistency in optimal fingerprinting. *Climate Dyn.*, **15**, 419–434, https://doi.org/10.1007/s003820050291.

Allen, R. J., and Coauthors, 2020: Climate and air quality impacts due to mitigation of non-methane near-term climate forcers. *Atmos. Chem. Phys.*, **20**, 9641–9663, https://doi.org/10.5194/acp-20-9641-2020.

Archer-Nicholls, S., and Coauthors, 2019: Radiative effects of residential sector emissions in China: Sensitivity to uncertainty in black carbon emissions. *J. Geophys. Res. Atmos.*, **124**, 5029–5044, https://doi.org/10.1029/2018JD030120.

Barnett, T., and Coauthors, 2005: Detecting and attributing external influences on the climate system: A review of recent advances. *J. Climate*, **18**, 1291–1314, https://doi.org/10.1175/JCLI3329.1.

Bi, D., and Coauthors, 2013: The ACCESS coupled model: Description, control climate and evaluation. *Aust. Meteor. Oceanogr. J.*, **63**, 41–64, https://doi.org/10.22499/2.6301.004.

——, and Coauthors, 2020: Configuration and spin-up of ACCESS-CM2, the new generation Australian Community Climate and Earth System Simulator coupled model. *J. South. Hemisphere Earth Syst. Sci.*, **70**, 225–251, https://doi.org/10.1071/ES19040.

Boucher, O., and Coauthors, 2013: Clouds and aerosols. *Climate Change 2013: The Physical Science Basis*, T. F. Stocker et al., Eds., Cambridge University Press, 571–658.

Chang, W., H. Liao, and H. Wang, 2009: Climate responses to direct radiative forcing of anthropogenic aerosols, tropospheric ozone, and long-lived greenhouse gases in eastern China over 1951–2000. *Adv. Atmos. Sci.*, **26**, 748–762, https://doi.org/10.1007/s00376-009-9032-4.

——, ——, J. Xin, Z. Li, D. Li, and X. Zhang, 2015: Uncertainties in anthropogenic aerosol concentrations and direct radiative forcing induced by emission inventories in eastern China. *Atmos. Res.*, **166**, 129–140, https://doi.org/10.1016/j.atmosres.2015.06.021.

Chang, W.-Y., and H. Liao, 2009: Anthropogenic direct radiative forcing of tropospheric ozone and aerosols from 1850 to 2000 estimated with IPCC AR5 emissions inventories. *Atmos. Ocean. Sci. Lett.*, **2**, 201–207, https://doi.org/10.1080/16742834.2009.11446804.

Chen, H., and Coauthors, 2020: Regional climate responses in East Asia to the black carbon aerosol direct effects from India and China in summer. *J. Climate*, **33**, 9783–9800, https://doi.org/10.1175/JCLI-D-19-0706.1.

Cherian, R., J. Quaas, M. Salzmann, and M. Wild, 2014: Pollution trends over Europe constrain global aerosol forcing as simulated by climate models. *Geophys. Res. Lett.*, **41**, 2176–2181, https://doi.org/10.1002/2013GL058715.

Danabasoglu, G., and Coauthors, 2020: The Community Earth System Model Version 2 (CESM2). *J. Adv. Model. Earth Syst.*, **12**, e2019MS001916, https://doi.org/10.1029/2019MS001916.

Dang, R., and H. Liao, 2019: Radiative forcing and health impact of aerosols and ozone in China as the consequence of clean air actions over 2012–2017. *Geophys. Res. Lett.*, **46**, 12 511–12 519, https://doi.org/10.1029/2019GL084605.

Dunne, J. P., and Coauthors, 2020: The GFDL Earth System Model version 4.1 (GFDL-ESM 4.1): Overall coupled model description and simulation characteristics. *J. Adv. Model. Earth Syst.*, **12**, e2019MS002015, https://doi.org/10.1029/2019MS002015.

Emmons, L. K., and Coauthors, 2020: The chemistry mechanism in the Community Earth System Model version 2 (CESM2). *J. Adv. Model. Earth Syst.*, **12**, e2019MS001882, https://doi.org/10.1029/2019MS001882.

Eyring, V., S. Bony, G. A. Meehl, C. A. Senior, B. Stevens, R. J. Stouffer, and K. E. Taylor, 2016: Overview of the Coupled Model Intercomparison Project Phase 6 (CMIP6) experimental design and organization. *Geosci. Model Dev.*, **9**, 1937–1958, https://doi.org/10.5194/gmd-9-1937-2016.

Flato, G., and Coauthors, 2013: Evaluation of climate models. *Climate Change 2013: The Physical Science Basis*, T. F. Stocker et al., Eds., Cambridge University Press, 741–866.

Gao, Y., B. Zhuang, T. Wang, H. Chen, S. Li, W. Wei, H. Lin, and M. Li, 2022: Climatic–environmental effects of aerosols and their sensitivity to aerosol mixing states in East Asia in winter. *Remote Sens.*, **14**, 3539, https://doi.org/10.3390/rs14153539.

Gillett, N. P., and Coauthors, 2016: The Detection and Attribution Model Intercomparison Project (DAMIP v1.0) contribution to CMIP6. *Geosci. Model Dev.*, **9**, 3685–3697, https://doi.org/10.5194/gmd-9-3685-2016.

Grandey, B. S., and Coauthors, 2018: Effective radiative forcing in the aerosol–climate model CAM5.3-MARC-ARG. *Atmos. Chem. Phys.*, **18**, 15 783–15 810, https://doi.org/10.5194/acp-18-15783-2018.

Hoesly, R. M., and Coauthors, 2018: Historical (1750–2014) anthropogenic emissions of reactive gases and aerosols from the Community Emissions Data System (CEDS). *Geosci. Model Dev.*, **11**, 369–408, https://doi.org/10.5194/gmd-11-369-2018.

Horowitz, L. W., and Coauthors, 2020: The GFDL global atmospheric chemistry-climate model AM4.1: Model description and simulation characteristics. *J. Adv. Model. Earth Syst.*, **12**, e2019MS002032, https://doi.org/10.1029/2019MS002032.

Hu, T., and Y. Sun, 2022: Anthropogenic influence on extreme temperatures in China based on CMIP6 models. *Int. J. Climatol.*, **42**, 2981–2995, https://doi.org/10.1002/joc.7402.

Kasoar, M., A. Voulgarakis, J.-F. Lamarque, D. T. Shindell, N. Bellouin, W. J. Collins, G. Faluvegi, and K. Tsigaridis, 2016: Regional and global temperature response to anthropogenic SO_2 emissions from China in three climate models. *Atmos. Chem. Phys.*, **16**, 9785–9804, https://doi.org/10.5194/acp-16-9785-2016.

Kelley, M., and Coauthors, 2020: GISS-E2.1: Configurations and climatology. *J. Adv. Model. Earth Syst.*, **12**, e2019MS002025, https://doi.org/10.1029/2019MS002025.

Klein, S. A., and A. Hall, 2015: Emergent constraints for cloud feedbacks. *Curr. Climate Change Rep.*, **1**, 276–287, https://doi.org/10.1007/s40641-015-0027-1.

Kuhlbrodt, T., and Coauthors, 2018: The low-resolution version of HadGEM3 GC3.1: Development and evaluation for global climate. *J. Adv. Model. Earth Syst.*, **10**, 2865–2888, https://doi.org/10.1029/2018MS001370.

Law, R. M., and Coauthors, 2017: The carbon cycle in the Australian Community Climate and Earth System Simulator (ACCESS-ESM1) – Part 1: Model description and pre-industrial simulation. *Geosci. Model Dev.*, **10**, 2567–2590, https://doi.org/10.5194/gmd-10-2567-2017.

Li, C., Z. Wang, F. Zwiers, and X. Zhang, 2021: Improving the estimation of human climate influence by selecting appropriate forcing simulations. *Geophys. Res. Lett.*, **48**, e2021GL095500, https://doi.org/10.1029/2021GL095500.

Li, J., Z. Han, and Z. Xie, 2013: Model analysis of long-term trends of aerosol concentrations and direct radiative forcings over East Asia. *Tellus*, **65B**, 20410, https://doi.org/10.3402/tellusb.v65i0.20410.

——, W.-C. Wang, Z. Sun, G. Wu, H. Liao, and Y. Liu, 2014: Decadal variation of East Asian radiative forcing due to anthropogenic aerosols during 1850–2100, and the role of atmospheric moisture. *Climate Res.*, **61**, 241–257, https://doi.org/10.3354/cr01236.

Li, K., H. Liao, J. Zhu, and J. M. Moch, 2016: Implications of RCP emissions on future $PM_{2.5}$ air quality and direct radiative forcing over China. *J. Geophys. Res. Atmos.*, **121**, 12 985–13 008, https://doi.org/10.1002/2016JD025623.

Liu, C., Y. Yang, H. Wang, L. Ren, J. Wei, P. Wang, and H. Liao, 2023: Influence of spatial dipole pattern in Asian aerosol changes on East Asian summer monsoon. *J. Climate*, **36**, 1575–1585, https://doi.org/10.1175/JCLI-D-22-0335.1.

Liu, R.-J., and H. Liao, 2017: Assessment of aerosol effective radiative forcing and surface air temperature response over eastern China in CMIP5 models. *Atmos. Ocean. Sci. Lett.*, **10**, 228–234, https://doi.org/10.1080/16742834.2017.1301188.

Liu, Y., M. Wang, Y. Qian, and A. Ding, 2022: A strong anthropogenic black carbon forcing constrained by pollution trends over China. *Geophys. Res. Lett.*, **49**, e2022GL098965, https://doi.org/10.1029/2022GL098965.

Lurton, T., and Coauthors, 2020: Implementation of the CMIP6 forcing data in the IPSL-CM6A-LR model. *J. Adv. Model. Earth Syst.*, **12**, e2019MS001940, https://doi.org/10.1029/2019MS001940.

Meinshausen, M., and Coauthors, 2017: Historical greenhouse gas concentrations for climate modelling (CMIP6). *Geosci. Model Dev.*, **10**, 2057–2116, https://doi.org/10.5194/gmd-10-2057-2017.

Michou, M., and Coauthors, 2020: Present-day and historical aerosol and ozone characteristics in CNRM CMIP6 simulations. *J. Adv. Model. Earth Syst.*, **12**, e2019MS001816, https://doi.org/10.1029/2019MS001816.

Myhre, G., and Coauthors, 2013a: Anthropogenic and natural radiative forcing. *Climate Change 2013: The Physical Science Basis*, T. F. Stocker et al., Eds., Cambridge University Press, 659–740.

——, and Coauthors, 2013b: Radiative forcing of the direct aerosol effect from AeroCom Phase II simulations. *Atmos. Chem. Phys.*, **13**, 1853–1877, https://doi.org/10.5194/acp-13-1853-2013.

Nie, Y., L. Li, Y. Tang, and B. Wang, 2019: Impacts of changes of external forcings from CMIP5 to CMIP6 on surface temperature in FGOALS-g2. *SOLA*, **15**, 211–215, https://doi.org/10.2151/sola.2019-038.

O'Connor, F. M., and Coauthors, 2021: Assessment of pre-industrial to present-day anthropogenic climate forcing in UKESM1. *Atmos. Chem. Phys.*, **21**, 1211–1243, https://doi.org/10.5194/acp-21-1211-2021.

Osborn, T. J., P. D. Jones, D. H. Lister, C. P. Morice, I. R. Simpson, J. P. Winn, E. Hogan, and I. C. Harris, 2021: Land surface air temperature variations across the globe updated to 2019: The CRUTEM5 data set. *J. Geophys. Res. Atmos.*, **126**, e2019JD032352, https://doi.org/10.1029/2019JD032352.

Oshima, N., S. Yukimoto, M. Deushi, T. Koshiro, H. Kawai, T. Y. Tanaka, and K. Yoshida, 2020: Global and Arctic effective radiative forcing of anthropogenic gases and aerosols in MRI-ESM2.0. *Prog. Earth Planet. Sci.*, **7**, 38, https://doi.org/10.1186/s40645-020-00348-w.

Pincus, R., P. M. Forster, and B. Stevens, 2016: The Radiative Forcing Model Intercomparison Project (RFMIP): Experimental protocol for CMIP6. *Geosci. Model Dev.*, **9**, 3447–3460, https://doi.org/10.5194/gmd-9-3447-2016.

Qi, Y., J. Ge, and J. Huang, 2013: Spatial and temporal distribution of MODIS and MISR aerosol optical depth over northern China and comparison with AERONET. *Chin. Sci. Bull.*, **58**, 2497–2506, https://doi.org/10.1007/s11434-013-5678-5.

Qian, Y., L. R. Leung, S. J. Ghan, and F. Giorgi, 2003: Regional climate effects of aerosols over China: Modeling and observation. *Tellus*, **55B**, 914–934, https://doi.org/10.3402/tellusb.v55i4.16379.

Randles, C. A., and Coauthors, 2013: Intercomparison of shortwave radiative transfer schemes in global aerosol modeling: Results from the AeroCom Radiative Transfer Experiment. *Atmos. Chem. Phys.*, **13**, 2347–2379, https://doi.org/10.5194/acp-13-2347-2013.

Remer, L. A., and Coauthors, 2005: The MODIS aerosol algorithm, products, and validation. *J. Atmos. Sci.*, **62**, 947–973, https://doi.org/10.1175/JAS3385.1.

Rotstayn, L. D., and J. E. Penner, 2001: Indirect aerosol forcing, quasi forcing, and climate response. *J. Climate*, **14**, 2960–2975, https://doi.org/10.1175/1520-0442(2001)014<2960:IAFQFA>2.0.CO;2.

Samset, B. H., 2022: Aerosol absorption has an underappreciated role in historical precipitation change. *Commun. Earth Environ.*, **3**, 242, https://doi.org/10.1038/s43247-022-00576-6.

——, and Coauthors, 2013: Black carbon vertical profiles strongly affect its radiative forcing uncertainty. *Atmos. Chem. Phys.*, **13**, 2423–2434, https://doi.org/10.5194/acp-13-2423-2013.

Schulz, M., and Coauthors, 2006: Radiative forcing by aerosols as derived from the AeroCom present-day and pre-industrial simulations. *Atmos. Chem. Phys.*, **6**, 5225–5246, https://doi.org/10.5194/acp-6-5225-2006.

Seland, Ø., and Coauthors, 2020: Overview of the Norwegian Earth System Model (NorESM2) and key climate response of CMIP6 DECK, historical, and scenario simulations. *Geosci. Model Dev.*, **13**, 6165–6200, https://doi.org/10.5194/gmd-13-6165-2020.

Seo, J., and Coauthors, 2020: The impacts of aerosol emissions on historical climate in UKESM1. *Atmosphere*, **11**, 1095, https://doi.org/10.3390/atmos11101095.

Seong, M.-G., S.-K. Min, Y.-H. Kim, X. Zhang, and Y. Sun, 2021: Anthropogenic greenhouse gas and aerosol contributions to extreme temperature changes during 1951–2015. *J. Climate*, **34**, 857–870, https://doi.org/10.1175/JCLI-D-19-1023.1.

Shindell, D., and G. Faluvegi, 2009: Climate response to regional radiative forcing during the twentieth century. *Nat. Geosci.*, **2**, 294–300, https://doi.org/10.1038/ngeo473.

——, M. Schulz, Y. Ming, T. Takemura, G. Faluvegi, and V. Ramaswamy, 2010: Spatial scales of climate response to inhomogeneous radiative forcing. *J. Geophys. Res.*, **115**, D19110, https://doi.org/10.1029/2010JD014108.

Shindell, D. T., 2014: Inhomogeneous forcing and transient climate sensitivity. *Nat. Climate Change*, **4**, 274–277, https://doi.org/10.1038/nclimate2136.

——, G. Faluvegi, L. Rotstayn, and G. Milly, 2015: Spatial patterns of radiative forcing and surface temperature response. *J. Geophys. Res. Atmos.*, **120**, 5385–5403, https://doi.org/10.1002/2014JD022752.

Smith, C. J., and P. M. Forster, 2021: Suppressed late-20th century warming in CMIP6 models explained by forcing and feedbacks. *Geophys. Res. Lett.*, **48**, e2021GL094948, https://doi.org/10.1029/2021GL094948.

——, and Coauthors, 2021: Energy budget constraints on the time history of aerosol forcing and climate sensitivity. *J. Geophys. Res. Atmos.*, **126**, e2020JD033622, https://doi.org/10.1029/2020JD033622.

Stier, P., and Coauthors, 2013: Host model uncertainties in aerosol radiative forcing estimates: Results from the AeroCom Prescribed intercomparison study. *Atmos. Chem. Phys.*, **13**, 3245–3270, https://doi.org/10.5194/acp-13-3245-2013.

Swart, N. C., and Coauthors, 2019: The Canadian Earth System Model version 5 (CanESM5.0.3). *Geosci. Model Dev.*, **12**, 4823–4873, https://doi.org/10.5194/gmd-12-4823-2019.

Tang, T., and Coauthors, 2020: Response of surface shortwave cloud radiative effect to greenhouse gases and aerosols and its impact on summer maximum temperature. *Atmos. Chem. Phys.*, **20**, 8251–8266, https://doi.org/10.5194/acp-20-8251-2020.

Tatebe, H., and Coauthors, 2019: Description and basic evaluation of simulated mean state, internal variability, and climate sensitivity in MIROC6. *Geosci. Model Dev.*, **12**, 2727–2765, https://doi.org/10.5194/gmd-12-2727-2019.

Turnock, S. T., and Coauthors, 2020: Historical and future changes in air pollutants from CMIP6 models. *Atmos. Chem. Phys.*, **20**, 14 547–14 579, https://doi.org/10.5194/acp-20-14547-2020.

Voulgarakis, A., and D. T. Shindell, 2010: Constraining the sensitivity of regional climate with the use of historical observations. *J. Climate*, **23**, 6068–6073, https://doi.org/10.1175/2010JCLI3623.1.

Wang, C.-S., Z.-L. Wang, Y.-D. Lei, H. Zhang, H.-Z. Che, and X.-Y. Zhang, 2022: Differences in East Asian summer monsoon responses to Asian aerosol forcing under different emission inventories. *Adv. Climate Change Res.*, **13**, 309–322, https://doi.org/10.1016/j.accre.2022.02.008.

Wang, H., T. Dai, M. Zhao, D. Goto, Q. Bao, T. Takemura, T. Nakajima, and G. Shi, 2020: Aerosol effective radiative forcing in the online aerosol coupled CAS-FGOALS-f3-L climate model. *Atmosphere*, **11**, 1115, https://doi.org/10.3390/atmos11101115.

Wang, Z., H. Zhang, and P. Lu, 2014: Improvement of cloud microphysics in the aerosol-climate model BCC_AGCM2.0.1_CUACE/Aero, evaluation against observations, and updated aerosol indirect effect. *J. Geophys. Res. Atmos.*, **119**, 8400–8417, https://doi.org/10.1002/2014JD021886.

——, and Coauthors, 2021: Incorrect Asian aerosols affecting the attribution and projection of regional climate change in CMIP6 models. *Climate Atmos. Sci.*, **4**, 2, https://doi.org/10.1038/s41612-020-00159-2.

Watson-Parris, D., and Coauthors, 2020: Constraining uncertainty in aerosol direct forcing. *Geophys. Res. Lett.*, **47**, e2020GL087141, https://doi.org/10.1029/2020GL087141.

Xu, Y., X. Gao, Y. Shi, and Z. Botao, 2015: Detection and attribution analysis of annual mean temperature changes in China. *Climate Res.*, **63**, 61–71, https://doi.org/10.3354/cr01283.

——, J. Wu, and Z. Han, 2022: Evaluation and projection of surface $PM_{2.5}$ and its exposure on population in Asia based on the CMIP6 GCMs. *Int. J. Environ. Res. Public Health*, **19**, 12092, https://doi.org/10.3390/ijerph191912092.

Yu, L., G. Leng, and Q. Tang, 2022: Varying contributions of greenhouse gases, aerosols and natural forcings to Arctic land surface air temperature changes. *Environ. Res. Lett.*, **17**, 124004, https://doi.org/10.1088/1748-9326/aca2c3.

Zanis, P., and Coauthors, 2020: Fast responses on pre-industrial climate from present-day aerosols in a CMIP6 multi-model study. *Atmos. Chem. Phys.*, **20**, 8381–8404, https://doi.org/10.5194/acp-20-8381-2020.

Zhang, H., S. Zhao, Z. Wang, X. Zhang, and L. Song, 2016: The updated effective radiative forcing of major anthropogenic aerosols and their effects on global climate at present and in the future. *Int. J. Climatol.*, **36**, 4029–4044, https://doi.org/10.1002/joc.4613.

Zhang, X., H. Wan, F. W. Zwiers, G. C. Hegerl, and S.-K. Min, 2013: Attributing intensification of precipitation extremes to human influence. *Geophys. Res. Lett.*, **40**, 5252–5257, https://doi.org/10.1002/grl.51010.

Ziehn, T., and Coauthors, 2020: The Australian Earth System Model: ACCESS-ESM1.5. *J. South. Hemisphere Earth Syst. Sci.*, **70**, 193–214, https://doi.org/10.1071/ES19035.